Cancellous bone and theropod dinosaur locomotion. Part III – Inferring posture and locomotor biomechanics in extinct theropods, and its evolution on the line to birds (#22655)

First submission

Editor guidance

Please submit by **7 Feb 2018** for the benefit of the authors (and your $200 publishing discount).

Structure and Criteria
Please read the 'Structure and Criteria' page for general guidance.

Author notes
Have you read the author notes on the guidance page?

Raw data check
Review the raw data. Download from the location described by the author.

Image check
Check that figures and images have not been inappropriately manipulated.

Privacy reminder: If uploading an annotated PDF, remove identifiable information to remain anonymous.

Files
Download and review all files from the materials page.

13 Figure file(s)
3 Table file(s)

Structure and Criteria

2

Structure your review

The review form is divided into 5 sections.
Please consider these when composing your review:

1. **BASIC REPORTING**
2. **EXPERIMENTAL DESIGN**
3. **VALIDITY OF THE FINDINGS**
4. General comments
5. Confidential notes to the editor

You can also annotate this PDF and upload it as part of your review

When ready submit online.

Editorial Criteria

Use these criteria points to structure your review. The full detailed editorial criteria is on your guidance page.

BASIC REPORTING

- Clear, unambiguous, professional English language used throughout.
- Intro & background to show context. Literature well referenced & relevant.
- Structure conforms to PeerJ standards, discipline norm, or improved for clarity.
- Figures are relevant, high quality, well labelled & described.
- Raw data supplied (see PeerJ policy).

EXPERIMENTAL DESIGN

- Original primary research within Scope of the journal.
- Research question well defined, relevant & meaningful. It is stated how the research fills an identified knowledge gap.
- Rigorous investigation performed to a high technical & ethical standard.
- Methods described with sufficient detail & information to replicate.

VALIDITY OF THE FINDINGS

- Impact and novelty not assessed. Negative/inconclusive results accepted. *Meaningful* replication encouraged where rationale & benefit to literature is clearly stated.
- Data is robust, statistically sound, & controlled.
- Conclusions are well stated, linked to original research question & limited to supporting results.
- Speculation is welcome, but should be identified as such.

Standout reviewing tips

The best reviewers use these techniques

Tip	*Example*
Support criticisms with evidence from the text or from other sources	*Smith et al (J of Methodology, 2005, V3, pp 123) have shown that the analysis you use in Lines 241-250 is not the most appropriate for this situation. Please explain why you used this method.*
Give specific suggestions on how to improve the manuscript	*Your introduction needs more detail. I suggest that you improve the description at lines 57- 86 to provide more justification for your study (specifically, you should expand upon the knowledge gap being filled).*
Comment on language and grammar issues	*The English language should be improved to ensure that an international audience can clearly understand your text. Some examples where the language could be improved include lines 23, 77, 121, 128 – the current phrasing makes comprehension difficult.*
Organize by importance of the issues, and number your points	*1. Your most important issue* *2. The next most important item* *3. …* *4. The least important points*
Please provide constructive criticism, and avoid personal opinions	*I thank you for providing the raw data, however your supplemental files need more descriptive metadata identifiers to be useful to future readers. Although your results are compelling, the data analysis should be improved in the following ways: AA, BB, CC*
Comment on strengths (as well as weaknesses) of the manuscript	*I commend the authors for their extensive data set, compiled over many years of detailed fieldwork. In addition, the manuscript is clearly written in professional, unambiguous language. If there is a weakness, it is in the statistical analysis (as I have noted above) which should be improved upon before Acceptance.*

Cancellous bone and theropod dinosaur locomotion. Part III – Inferring posture and locomotor biomechanics in extinct theropods, and its evolution on the line to birds

Peter Bishop Corresp., [1] , **Scott Hocknull** [1] , **Christofer Clemente** [2] , **John Hutchinson** [3] , **Andrew Farke** [4] , **Rod Barrett** [5] , **David Lloyd** [5]

[1] Geosciences Program, Queensland Museum, Brisbane, Queensland, Australia

[2] School of Science and Engineering, University of the Sunshine Coast, Maroochydore, Queensland, Australia

[3] Department of Comparative Biomedical Sciences, Royal Veterinary College, Hatfield, Hertfordshire, United Kingdom

[4] Raymond M. Alf Museum of Paleontology at The Webb Schools, Claremont, California, United States of America

[5] School of Allied Health Sciences, Griffith University, Gold Coast, Queensland, Australia

Corresponding Author: Peter Bishop
Email address: peter.bishop@qm.qld.gov.au

This three-part series investigates the architecture of cancellous bone in the main hindlimb bones of theropod dinosaurs, and uses cancellous bone architectural patterns to infer locomotor biomechanics in extinct non-avian species. Cancellous bone is highly sensitive to its prevailing mechanical environment, and may therefore help further understanding of locomotor biomechanics in extinct tetrapod vertebrates such as dinosaurs. Here in Part III, the biomechanical modelling approach derived previously was applied to two species of extinct, non-avian theropods, Daspletosaurus torosus and Troodon formosus. Observed cancellous bone architectural patterns were linked with quasi-static, three-dimensional musculoskeletal and finite element models of the hindlimb of both species, and used to derive characteristic postures that best aligned continuum-level principal stresses with cancellous bone fabric. The posture identified for Daspletosaurus was largely upright, with a subvertical femoral orientation, whilst that identified for Troodon was more crouched, but not to the degree observed in extant birds. In addition to providing new insight on posture and limb articulation, this study also tested previous hypotheses of limb bone loading mechanics and muscular control strategies in non-avian theropods, and how these aspects evolved on the line to birds. The results support the hypothesis that an upright femoral posture is correlated with bending-dominant bone loading and abduction-based muscular support of the hip, whereas a crouched femoral posture is correlated with torsion-dominant bone loading and long-axis rotation-based muscular support. Moreover, the results of this study also support the inference that hindlimb posture, bone loading mechanics and muscular support strategies evolved in a gradual fashion along the line to extant birds.

Cancellous bone and theropod dinosaur locomotion. Part III – Inferring posture and locomotor biomechanics in extinct theropods, and its evolution on the line to birds

P.J. Bishop[1,2,3,*], S.A. Hocknull[1,2,3], C.J. Clemente[4,5], J.R. Hutchinson[6], A.A. Farke[7], R.S. Barrett[2,3] and D.G. Lloyd[2,3].

[1]Geosciences Program, Queensland Museum, Brisbane, Queensland, Australia.
[2]School of Allied Health Sciences, Griffith University, Gold Coast, Queensland, Australia.
[3]Innovations in Health Technology, Menzies Health Institute Queensland.
[4]School of Science and Engineering, University of the Sunshine Coast, Maroochydore, Queensland, Australia.
[5]School of Biological Sciences, The University of Queensland, Brisbane, Queensland, Australia.
[6]Structure and Motion Laboratory, Department of Comparative Biomedical Sciences, Royal Veterinary College, Hatfield, Hertfordshire, UK.
[7]Raymond M. Alf Museum of Paleontology at The Webb Schools, Claremont, California, USA.

*corresponding author: peter.bishop@qm.qld.gov.au.

III.1 Abstract

This three-part series investigates the architecture of cancellous bone in the main hindlimb bones of theropod dinosaurs, and uses cancellous bone architectural patterns to infer locomotor biomechanics in extinct non-avian species. Cancellous bone is highly sensitive to its prevailing mechanical environment, and may therefore help further understanding of locomotor biomechanics in extinct tetrapod vertebrates such as dinosaurs. Here in Part III, the biomechanical modelling approach derived previously was applied to two species of extinct, non-avian theropods, *Daspletosaurus torosus* and *Troodon formosus*. Observed cancellous bone architectural patterns were linked with quasi-static, three-dimensional musculoskeletal and finite element models of the hindlimb of both species, and used to derive characteristic postures that best aligned continuum-level principal stresses with cancellous bone fabric. The posture identified for *Daspletosaurus* was largely upright, with a subvertical femoral orientation, whilst that identified for *Troodon* was more crouched, but not to the degree observed in extant birds. In addition to providing new insight on posture and limb articulation, this study also tested previous hypotheses of limb bone loading mechanics and muscular control strategies in non-avian theropods, and how these aspects evolved on the line to birds. The results support the hypothesis that an upright femoral posture is correlated with bending-dominant bone loading and abduction-based muscular support of the hip, whereas a crouched femoral posture is correlated with torsion-dominant bone loading and long-axis rotation-based muscular support. Moreover, the results of this study also support the inference that hindlimb posture, bone loading mechanics and muscular support strategies evolved in a gradual fashion along the line to extant birds.

III.2 Introduction

The non-avian theropod dinosaurs include some of the most recognisable of extinct animals, and ~~owing to such factors as~~ the carnivorous lifestyle and large body size of many species, they have received much attention concerning various aspects of their palaeobiology (e.g., Alexander 1989; Bakker 1986; Brusatte et al. 2010; Horner & Lessem 1993; Molnar & Farlow 1990). Locomotion in particular is a well-studied (and sometimes controversial) topic, not only because of the interest in how a giant, bipedal predator may have functioned, but also because it was likely intimately tied to the evolution of the living decendants of non-avian dinosaurs, the volant birds (Allen et al. 2013; Gatesy 1990; Gatesy 1995; Gatesy 2002; Gatesy & Middleton 1997; Hutchinson & Allen 2009). A variety of different approaches and lines of evidence have been previouly used to address questions of locomotor biomechanics in non-avian theropods and its evolution on the line to birds, including fossil footprints (Farlow et al. 2012; Gatesy et al. 1999; Thulborn 1990), external bone shapes and proportions (Carrano 1998; Carrano 2000; Gatesy & Middleton 1997; Paul 1998), bone scaling (Carrano 2001; Christiansen 1999; Gatesy 1991), midshaft cortical geometry (Alexander 1989; Christiansen 1998; Farlow et al. 1995) and muscle attachments and significance (Carrano & Hutchinson 2002; Gatesy 1990; Hutchinson 2001a; Hutchinson 2001b). These have been more recently supplemented with various computational biomechanical models, that have examined aspects such as speed capabilities (Gatesy et al. 2009; Hutchinson 2004; Hutchinson & Garcia 2002; Sellers & Manning 2007), muscle moment arms (Bates & Schachner 2012; Bates et al. 2012; Hutchinson et al. 2005; Hutchinson et al. 2008) and mass properties (Allen et al. 2013; Allen et al. 2009; Bates et al. 2012; Bates et al. 2009a; Bates et al. 2009b; Henderson 1999; Henderson & Snively 2003; Hutchinson et al. 2007)

The collective result of this prolonged and intensive research focus has been a much refined understanding of how anatomy influenced non-avian theropod stance and gait, and how these may have evolved on the line to extant birds. For instance, most non-avian species are inferred to have used a largely upright hindlimb posture during normal locomotion, where the hips and knees were flexed only to a minor degree; however, more crownward clades (e.g., paravians) may have used a more crouched posture with greater flexion at the hip and knee (Hutchinson & Allen

2009). These postural changes are inferred to have occurred in association with changes in other biomechanically important aspects, including an anterior shift in the location of the whole-body centre of mass (COM; Allen et al. 2013), the muscular mechanisms of limb support and propulsion (Gatesy 1990; Gatesy 1995; Gatesy 2002; Hutchinson & Gatesy 2000) and bone loading mechanics (Carrano 1998). Yet, despite ~~the~~ important advances in understanding ~~made~~, there is still potential for further advances to be made, from investigation of hitherto unstudied lines of evidence. One such line of evidence is the architecture of cancellous bone, which is well known from studies of extant animals to be highly sensitive and well adapted to its prevailing mechanical environment (cf. Part I of this series; Bishop et al. in review-c). Study of cancellous bone architectural patterns in non-avian theropods may therefore provide new and unique insight into various aspects of non-avian theropod locomotor biomechanics.

In Part I of this series, stark differences in hindlimb cancellous bone architecture were found between humans and birds, the only obligate bipeds alive today. Many of these differences can be associated with differences in the manner of striding, parasagittal, bipedal locomotion employed by the two groups. In particular, the differences in cancellous bone architecture reflect differences in their upright *versus* crouched postures and subsequent whole-bone loading mechanics, that is, the prominence of bending and torsion. The different postures employed by humans and birds are also associated with the mechanism of muscular control required to achieve limb support during locomotion. In humans, mediolateral collapse of the stance phase limb is counteracted by hip abduction, conferred predominantly by the gluteal muscles located dorsal to the hip (Pauwels 1980; Wall-Scheffler et al. 2010). However, in birds, anatomical, kinematic and electromyographic evidence suggests that stance limb collapse is counteracted predominantly by medial (internal) long-axis rotation of the subhorizontally oriented femur, conferred by the iliotrochantericus muscles located anterior to the hip (Gatesy 1999b; Hutchinson & Gatesy 2000). But what of extinct obligate bipeds, such as non-avian theropod dinosaurs?

In ~~more plesiomorphic~~ species of non-avian theropod, the architecture of cancellous bone in the main hindlimb bones exhibits much similarity to that of humans, in terms of both principal fabric directions in the hip and knee and whole-bone architectural patterns. In more phylogenetically derived species, however, cancellous bone architecture tended to be more similar to that observed

in extant birds (Part I; Bishop et al. in review-c). Given that cancellous bone architectures in extant obligate bipeds appear to be linked to their different locomotor biomechanics, these observations raise the following questions regarding non-avian theropods:

1. Did the different species of non-avian theropods employ different limb postures?
2. Did the bones of the different species of non-avian theropods experience different loading regimes?
3. Did the different species of non-avian theropods employ different strategies of muscular support in counteracting stance limb collapse?
4. If the different species of non-avian theropods did employ different suites of hindlimb locomotor biomechanics, how did these evolve on the line to extant birds?

Previously, the integration of anatomical, kinematic, bone strain and electromyographic data in extant species led Carrano (1998) and Hutchinson & Gatesy (2000) to hypothesize that the aforementioned aspects of bipedal locomotor biomechanics were intimately tied throughout theropod evolution. The incremental change of external osteological features throughout theropod evolution was also taken to indicate that the transformation in these particular biomechanical aspects was a gradual occurrence (Hutchinson 2001a; Hutchinson 2001b; Hutchinson & Gatesy 2000). More broadly however, the exact ~~nature~~ of theropod locomotor evolution, in terms of whether it was long and gradual, or more punctuated at certain instances, remains to be fully discerned (Allen et al. 2013; Hutchinson & Allen 2009).

A new approach that can quantitatively address the aforementioned questions was outlined in Part II of this series (Bishop et al. in review-b). In this 'reverse trajectorial approach', the observed three-dimensional (3-D) architecture of cancellous bone in the main bones of the hindlimb is coupled with musculoskeletal and finite element models of the hindlimb. Under a quasi-static situation, these models are used to derive a single 'characteristic posture', one in which continuum-level principal stresses best align with cancellous bone fabric. This characteristic posture is a time- and load-averaged posture across all loading regimes, and it is important to recognize that it may or may not be an actual posture used at a particular instance in a particular behaviour.

In Part II it was shown that when applied to an extant theropod (chicken, *Gallus gallus*), the new approach was able to retrieve a posture that was quite comparable to that used by birds at around the midstance of normal terrestrial locomotion. It could also provide a reasonable assessment of bone loading in the proximal limb (i.e., femur, proximal tibia and proximal fibula) and muscle control strategies for limb stabilization, although it had markedly lower accuracy in terms of bone loading in the distal limb (tibial shaft and below) and muscle control strategies for limb propulsion. Additionally, it was shown that the results of this approach were largely insensitive to actual muscle size (manifest as force-generating capacity), a key unknown for extinct species. When applied to extinct, non-avian theropods, the approach may therefore be used to investigate posture, bone loading mechanics and muscle recruitment patterns in these species as well. Thus, in this approach the architecture of cancellous bone constitutes an independent data set against which one or more biomechanical hypotheses may be tested.

The present study aimed to quantitatively test the hypotheses of Carrano (1998) and Hutchinson & Gatesy (2000) concerning the evolution of theropod locomotor mechanics. To do this, it applied the reverse trajectorial approach to two species of non-avian theropod, the basal coelurosaur *Daspletosaurus torosus* and the derived paravian *Troodon formosus* (cf. Fig. 8 of Part I), to derive a single characteristic hindlimb posture that best reflects these species' architectural patterns of cancellous bone. These species show markedly different cancellous bone architectures, with that of the former more similar to that of humans and that of the latter bearing stronger resemblance to that of birds (Part I). Understanding limb posture in these and other non-avian theropod species is in and of itself important, but it is also important for understanding other aspects of locomotion. For instance, posture can influence maximum speed capability in bipeds (Gatesy et al. 2009; Hutchinson 2004; Hutchinson & Allen 2009). In concert with the results already derived from for an extant bird, the chicken (Part II), the results of this study will also facilitate an examination of how locomotor biomechanics has evolved in theropods on the line to extant birds.

III.3 Materials and Methods

The methodology employed in the present study followed that outlined previously in Part II (Bishop et al. in review-b). Essentially, musculoskeletal models of the hindlimb in a static posture were used to provide the force and boundary conditions for finite element modelling of the individual limb bones, from which principal stress trajectories were determined and compared to cancellous bone architectural patterns. Only those differences associated with the modelling of the two different species will be described in the present study. Also, as with the previous study, all assumptions and model parameters were kept in their 'best guess' manifestation throughout the analyses; thus, differences in model results directly reflected differences in limb postures in the extinct species.

III.3.1 Skeletal geometry acquisition

The models developed in this study were derived through a combination of X-ray computed tomographic (CT) scanning and photogrammetry of multiple fossil specimens; see Table 1 for the specimens (and institutional abbreviations) and imaging parameters used. The CT scans for each specimen were segmented using the software Mimics 17.0 (Materialize NV, Belgium), via a combination of manual and automatic techniques, to produce initial surface meshes of each bone. For photogrammetry, digital photographs were taken with a Lumix DMC-TZ40 (Panasonic, Japan) and rendered to produce 3-D meshes using the software Agisoft Photoscan 1.0.4 (Agisoft LLC, Russia), RealityCapture 1.0 (Capturing Reality s.r.o., Slovakia), Meshlab 1.3.3 (http://meshlab.sourceforge.net/) and CloudCompare 2.5.4 (http://www.cloudcompare.org/).

To maximize rigour, the models for each species were based primarily on single focal individuals that were relatively complete and well-preserved, and for which information on cancellous bone architecture was previously reported (Part I). These were TMP 2001.036.0001 for *Daspletosaurus* and MOR 748 for *Troodon*. At the time the research was undertaken, the specimens used to produce the model for *Troodon* were believed to represent a single species, *Troodon formosus*. However, recent research has indicated otherwise, and furthermore has cast doubt on the validity of the name *Troodon formosus* itself (van der Reest & Currie 2017); the majority of specimens used in this study therefore belong to an unnamed taxon. Nonetheless, the

model constructed here is still considered to be an accurate reflection of the anatomy of a large, derived North American troodontid. Moreover, for the sake of simplicity in the present study, the animal being modelled will herein be referred to as '*Troodon*'.

Some bones, or parts thereof, were missing from these focal specimens, and in these cases their geometry was modelled using other specimens of the same or closely related species (Table 1). This was achieved by scaling the geometries of these other specimens appropriately to fit the focal specimens' bones, accomplished using a combination of Mimics and the computer-aided design software Rhinoceros 4.0 (McNeel, USA). Wholesale reconstruction was required for the much of the pubis in *Daspletosaurus* and much of the ilium in '*Troodon*'. In *Daspletosaurus*, the general shape of the pubis was evident from the focal specimen, but much of the boot, pubic apron and ischiadic head were reconstructed based on comparison to other specimens that were imaged (Table 1), personal observation of other specimens in the TMP and MOR collections, and also the tyrannosaurid literature (e.g., Brochu 2003; Osborn 1917). In '*Troodon*', the acetabulum, antitrochanter and pubic and ischiadic peduncles were present in the focal specimen, but the anterior and posterior iliac blades were reconstructed based on comparison to other troodontids described in the literature (e.g., Gao et al. 2012; Tsuihiji et al. 2014; Xu et al. 2002). The assembly of the individual elements of the pelvis was based on the geometry of individual bones, but also on specimens of other tyrannosaurids or paravians where the pelvic elements were preserved *in situ* and intact with the sacrum (e.g., Brochu 2003; Gao et al. 2012; Lambe 1917; Norell & Makovicky 1997; Osborn 1917; Tsuihiji et al. 2014; Xu et al. 2002), as well as personal observation of other specimens in the TMP and MOR collections and displays. For completeness, the vertebral column was represented by a single cylinder fixed with respect to the pelvis. In addition to the pelvis, the distalmost fibular shaft was also reconstructed for '*Troodon*'; it was essentially a continuation of the preserved part of the shaft, tapering towards the end, and gently curving laterally as it approaches the distal tibia (cf. Norell & Makovicky 1999; Ostrom 1969).

Some of the individual bones used in the above procedure had undergone a variable amount of taphonomic distortion. However, in all cases this appeared to be brittle deformation only, in the form of fracturing and rigid displacement of the fragments relative to one another. In these instances, the bones were retro-deformed in Rhinoceros, under the assumption of brittle

deformation (Lautenschlager 2016). This rigid retro-deformation restored the fossil geometry closer to the original geometry by realigning fragments along apposing fracture surfaces, and also taking into consideration the geometry of the bones in other specimens and other species, including comparison to the literature (e.g., Brochu 2003; Tsuihiji et al. 2014). The retro-deformed geometries were then 'smoothed over' in Mimics and 3-Matic 9.0 (Materialize NV, Belgium). Additionally, cracks or abraded edges were filled in and reconstructed in Mimics; only the minimal amount of filling in required was undertaken.

Once an initial surface mesh had been produced for the complete geometry of each bone for both species, these were smoothed in 3-matic and then refined to produce a more isoparametric mesh in ReMESH 2.1 (Attene & Falcidieno 2006; http://remesh.sourceforge.net/). Although the tibia, astragalus and calcaneum typically remain as separate ossifications in tyrannosaurids, and the tibia remains separate from the astragalus and calcaneum in troodontids, the meshes of the three bones were fused together in this study to create a single tibiotarsus geometry. This was undertaken for the sake of simplifying the models, as well as maintaining a greater degree of consistency with the previously developed chicken model of Part II.

III.3.2 Musculoskeletal modelling

Musculoskeletal models of the right hindlimb of *Daspletosaurus* and '*Troodon*' were constructed in NMSBuilder (Martelli et al. 2011; Valente et al. 2014) for use in OpenSim 3.0.1 (Delp et al. 2007), and are shown in Figs 1 and 2. Both comprised 12 degrees of freedom, as in the chicken model of Part II, and 38 musculotendon actuators.

III.3.2.1 Definition of joints

Joint locations and orientations were defined in a similar fashion to the chicken model. However, the location of the hip joint was left open-ended, so as to investigate the effects of different hip articulations (see Section III.3.4 below). Initially, the centre of the joint in the femur was

276 determined by fitting a sphere to the femoral head in 3-matic, and the centre of the joint in the
277 acetabulum was determined by positioning the centre of femoral head sphere in the centre of the
278 acetabulum (in both lateral and anterior views). Hence, in this initial configuration, the
279 articulation of the femur with the acetabulum was consistent with the configuration used for the
280 chicken model. It was also consistent with the inference drawn in Part I from observations of
281 cancellous bone architecture (Section I.5.2.3), that the articulation was possibly centred about the
282 apex of the femoral head. The articulation of the tibia and fibula was guided by the relative
283 positions of the fibular crest on the tibiotarsus and the flared anteromedial process of the
284 proximal fibula, as well as the facet formed distally by the tibia, astragalus and calcaneum for
285 reception of the fibula. As with the chicken model, the pes was modelled as a rectangular prism,
286 with a width set to the mediolateral width of the distal tarsometatarsus and a length set to the total
287 length of digit III; the total length of digit III for the '*Troodon*' model was based on the data of
288 Russell (1969) for *Latenivenatrix mcmasterae*, scaled to the individual modelled in the current
289 study.
290
291
292 III.3.2.2 Definition of muscle and ligament anatomy
293
294 The hindlimb myology of *Daspletosaurus* and '*Troodon*' was reconstructed through analysis of
295 the muscle and ligament scarring patterns observed on the fossil bones, framed in the context of
296 the myology and scarring patterns of extant archosaurs (Bates & Schachner 2012; Bates et al.
297 2012; Carrano & Hutchinson 2002; Hutchinson 2001a; Hutchinson 2001b; Hutchinson 2002;
298 Hutchinson et al. 2005; Hutchinson et al. 2008). The 33 muscles and four ligaments
299 reconstructed, along with their origins and insertions, are listed in Table 2. As in the chicken
300 model, the collateral ligaments of the knee and ankle were represented by four musculotendon
301 actuators in both the *Daspletosaurus* and '*Troodon*' models. Each muscle was represented by a
302 single musculotendon actuator in the models, with one exception; the iliotibialis 2 (IT2) was
303 represented by two actuators on account of its probable expansive origin on the dorsal ilium
304 (Bates et al. 2012; Hutchinson et al. 2005; Hutchinson et al. 2008). The 3-D courses of the
305 actuators were constrained to follow paths that are comparable to those reported for homologous

muscles in extant archosaurs, and also as reconstructed for other non-avian theropod species (Bates & Schachner 2012; Bates et al. 2012; Hutchinson et al. 2005; Hutchinson et al. 2008).

In reconstructing the muscular and ligamentous components of the models, a number of simplifying assumptions were made. Two muscles, the ambiens (AMB) and fibularis longus (FL) may possibly have sent off secondary tendons to attach more distally in the limb, as can occur in extant archosaurs (Carrano & Hutchinson 2002; Hutchinson 2002). However, these secondary attachments were assumed to be of little importance for bone loading mechanics as far as the present study is concerned, and so were not modelled. A distal accessory tendon was considered to be absent from the caudofemoralis longus (CFL), as the fourth trochanter of both species lacks a distally directed process or is of small size (Carrano & Hutchinson 2002; Hutchinson 2001a). It is also possible that there may have been other flexor muscles of digits II–IV in both *Daspletosaurus* and '*Troodon*', in addition to the flexores digitorum longus (FDL) et brevis (FDB), but currently it is too speculative to infer these (Carrano & Hutchinson 2002; Hutchinson 2002). It was assumed in the present study that if any such digital flexor muscles were present in either species, they would have had a similar disposition to the FDL, and so their action could be represented by the FDL actuator.

III.3.2.3 Definition of segment mass properties

To estimate the mass properties of each limb segment in the *Daspletosaurus* musculoskeletal model, the segment soft tissue models of Allen et al. (2013) for *Tyrannosaurus* were modified appropriately to fit the pelvic and limb elements of *Daspletosaurus*. This was accomplished in Rhinoceros. Likewise, the segment soft tissue models of Allen et al. (2013) for *Velociraptor* were modified appropriately to fit the pelvic and limb elements of '*Troodon*' in the estimation of mass properties in its model. The application of the soft tissue models developed for other species to the species studied here is justified, due to close phylogenetic relationship and much similarity in the underlying skeletal structure between the species involved. Assuming a bulk density of 1000 kg/m^3 for all body segments, the total mass of the right hindlimb in the *Daspletosaurus* model was calculated to be 342.7 kg, and that in the '*Troodon*' model was 5.65 kg.

337

338 To completely define the musculoskeletal model, this also required the calculation of mass
339 properties for the remainder of the body, that is, the pelvis segment of the models. Based on
340 femoral mid-shaft circumferences, equation 7 of Campione et al. (2014) was used to estimate the
341 total body mass for the two models. This resulted in a mass of 2757 kg for the *Daspletosaurus*
342 model and 48.5 kg for the '*Troodon*' model, and hence the mass of the pelvis segment in the two
343 models (including the mass of the left hindlimb) was 2414.3 kg and 42.85 kg, respectively. By
344 unintended coincidence, in both models the mass of the right hindlimb constituted approximately
345 12% of total body weight, which therefore increased consistency between two models. For
346 comparison, the mass of the hindlimb in the chicken model of Part II constituted approximately
347 10% of total body weight. Given the data reported by Allen et al. (2013), the combined COM of
348 the whole body, minus the right leg, in their 'average' model of *Tyrannosaurus* was 0.544 m
349 anterior to the hip joint. The femur length of the specimen upon which their model was based is
350 1.265 m, as reported by Hutchinson et al. (2011). Scaling isometrically to the *Daspletosaurus*
351 model, which has a femur length of 0.984 m, the COM of the pelvis segment was set at 0.423 m
352 anterior to the hip. Similarly, the combined COM of the whole body, minus the right leg, in the
353 'average' *Velociraptor* model of Allen et al. (2013) was 0.090 m anterior to the hip joint, and the
354 femur length upon which their model was based is 0.163 m. Thus, scaling isometrically to the
355 '*Troodon*' model, which has a femur length of 0.304 m, the COM of the pelvis segment was set
356 at 0.168 m anterior to the hip. The dorsoventral position of the COM of the pelvis segment was
357 assumed to be level with the hip. As noted in Part II, the dorsoventral position of the pelvis
358 segment COM will not influence the results so long as the pelvis segment's orientation was fixed
359 in all simulations, and all simulations were quasi-static in nature.

360

361

362 III.3.2.4 Muscle activity

363

364 Not all of the 34 musculotendon actuators representing muscles were set to be active during the
365 musculoskeletal simulations, in both *Daspletosaurus* and '*Troodon*' (Table 3). The inactive
366 muscles were set using the same criteria employed for the chicken model, and through
367 comparison to published electromyography data for homologous hindlimb muscles in extant

archosaurs (Gatesy 1990; Gatesy 1994; Gatesy 1997; Gatesy 1999b; Jacobson & Hollyday 1982; Marsh et al. 2004; Reilly & Blob 2003; Roberts et al. 1998). One exception to this was the iliofemoralis externus (IFE), which in both birds and crocodilians is mostly active during the swing phase of locomotion. However, in the evolutionary scenario proposed by Hutchinson & Gatesy (2000), abductor muscles such as the IFE are expected to have been crucial to maintaining stance limb stability, if the femur was habitually held in the subvertical orientation hypothesized for most, if not all, non-avian theropods (Hutchinson & Allen 2009). Moreover, the hypothesis of Hutchinson & Gatesy (2000) explains the stance phase inactivity of the IFE (or its homologues) in birds and crocodilians as a result of other hip muscles conferring stance limb support, namely, medial long-axis rotators in birds (iliotrochanterici) and adductors in crocodilians (adductores femoris 1 et 2). Thus, to test the hypothesis of Hutchinson & Gatesy (2000) among others, the IFE was set as being active in both the *Daspletosaurus* and '*Troodon*' simulations. All active musculotendon actuators were assigned the same maximum force capacity, equal to two times body weight, that is, 54073.9 N for *Daspletosaurus* and 951.2 N for '*Troodon*'.

As in the chicken simulations of Part II, a reserve actuator was applied to the metatarsophalangeal joint in the musculoskeletal simulations. The maximum output of this actuator in the *Daspletosaurus* and '*Troodon*' simulations was scaled from that set for the chicken (1,000 Nm), in proportion to the total body mass of each model: 1,767,308 Nm for *Daspletosaurus* and 31,090 Nm for '*Troodon*'. This corresponds to a minimum of 27 times the product of body weight and total hindlimb length (sum of interarticular lengths of femur, tibiotarsus and tarsometatarsus). By providing ample control of the metatarsophalangeal joint, this helped reduce excessively high recruitment of the FDL and FDB.

III.3.2.5 Initial posture

A general mid-stance posture was used as an initial starting point, which was modified in subsequent modelling iterations, as per the process outlined in Part II of this study. This initial posture was based on general interpretations of tyrannosaurid and troodontid appearance in the literature (technical and popular). Additionally, the hip extension angle was initially set so that

399 the knee joint was near the line of the vertical ground reaction force in the *x*-*z* (sagittal) plane,
400 following previous interpretations of theropod hindlimb biomechanics (Gatesy et al. 2009;
401 Hutchinson & Gatesy 2006).
402
403
404 ***III.3.3 Finite element modelling***
405
406 Finite element simulations of the *Daspletosaurus* and '*Troodon*' models were developed and
407 solved in largely the same manner as the previously described chicken simulations of Part II,
408 using ANSYS 17.0 (Ansys, Inc., USA). Two minor differences were that (i) a graduated and finer
409 mesh was used around the cleft of the lesser trochanter of the *Daspletosaurus* femur, to reduce
410 stress artifacts, and (ii) connection between the tibiotarsus and fibula entities was modelled both
411 proximally and distally. The latter difference reflects that fact that both tyrannosaurs and
412 troodontids possessed a distinct furrow in the distal tibiotarsus for reception of the distal fibula,
413 whereas in birds the distal fibula is greatly reduced. In the *Daspletosaurus* model, the total
414 number of elements used across the various postures tested ranged from 961,023 to 975,544 in
415 the femur simulation and from 985,071 to 1,005,550 in the tibiotarsus + fibula simulation. In the
416 '*Troodon*' model, the total number of elements used across the various postures tested ranged
417 from 668,033 to 684,547 in the femur simulation and from 583,228 to 598,556 in the tibiotarsus
418 + fibula simulation.
419
420
421 ***III.3.4 Varying hip articulation***
422
423 Following the identification of a 'solution posture' for the *Daspletosaurus* model, a brief
424 exploratory exercise was undertaken to address the ambiguity surrounding the articulation of
425 non-avian theropod hips. Unlike birds, many non-avian theropods typically possessed a large
426 incongruence in size between the femoral head and the acetabulum; for example, in the
427 *Daspletosaurus* focal specimen studied, the diameter of the femoral head is about two-thirds that
428 of the acetabulum (Fig. 3). This has consequently created uncertainty in exactly how the femur
429 articulated with the acetabulum in these extinct species. It has been previously suggested that the

main area of articulation on the femur occurred on the roughly cylindrical part of the femoral head, lateral to the apex of the head (e.g., Hotton 1980; Hutchinson & Allen 2009). However, cancellous bone architectural patterns observed in *Allosaurus* and tyrannosaurids (Part I) suggest that hip joint loads may have been transmitted through the femoral head mainly from the apex of the head, not from the more lateral parts.

To examine the effect of different hip articulations in the *Daspletosaurus* model, this was varied to assess if any improvement in correspondence between principal stress trajectories and cancellous bone architecture was possible beyond that of the solution posture (Fig. 3). Two such variations were made. Firstly, the femur was moved 50 mm medially with respect to the acetabulum, so that a sizeable proportion of the cylindrical part of the femoral head was in close proximity to the acetabulum (Fig. 3C,D). The rest of the limb was also moved medially along with the femur, including the coordinate systems of distal joints and all musculotendon actuator origins, insertions and via points that were level with or distal to the hip. So as to maintain a similar mediolateral foot placement as the original solution posture, the amount of hip abduction-adduction was altered slightly. In the second variation, the femur and limb distal to it was again moved 50 mm medially with respect to the acetabulum, but the hip was also abducted by 14°, producing a net 10° abduction from the neutral posture (Fig. 3E,F). This reflects the amount of hip abduction that has been supposed for tyrannosaurids in previous modelling studies (e.g., Hutchinson et al., 2005, 2007), on account of the inclined disposition of the femoral head relative to the long-axis of the femur. In order to bring the foot anywhere near the body midline, this abducted posture also necessitated a large 27° of external long-axis rotation of the hip, a value comparable to maximal external long-axis rotation in modern birds during straight-line locomotion (Kambic et al. 2015; Rubenson et al. 2007).

III.3.5 Cross-species patterns

Once solution postures were identified for both the *Daspletosaurus* and '*Troodon*' models, a number of biomechanically relevant parameters were extracted. The same parameters were also extracted from the solution posture identified previously for the chicken model of Part II. By way

of comparison across the three species, these parameters would allow a quantitative assessment of the evolutionary-biomechanical hypotheses of Carrano (1998) and Hutchinson & Gatesy (2000). Three sets of parameters were extracted:

1. *Postural parameters*, related to Question 1 posed in the Introduction: the location of the whole-body COM as normalized by total hindlimb length, joint angles for the hip and knee, and the 'degree of crouch', both actual and predicted from empirical data reported by Bishop et al. (in review-a).
2. *Bone loading parameters*, related to Question 2 posed in the Introduction: the orientation of principal stresses at the femoral mid-shaft, the ratio of maximum shear stress to bending stresses at the femoral mid-shaft, and the orientation of the neutral axis of bending at the femoral mid-shaft, relative to the mediolateral axis. To enable estimation of these parameters at mid-shaft, a local long-axis in the vicinity of the mid-point of the bone was determined. This was calculated by fitting a cylinder to the shaft in the immediate vicinity of the mid-point, calculated in 3-matic; the long-axis of the cylinder defined the local long-axis of the bone, and the plane normal to this axis defined the plane of the mid-shaft cross-section. The orientation of principal stresses was defined as the orientation of the steepest inclined stress vector with respect to the local long-axis; this was calculated separately for both $\boldsymbol{\sigma}_1$ and $\boldsymbol{\sigma}_3$, and then the mean orientation was taken. In pure bending the orientation would be 0°, that is, parallel to the long-axis, and in pure torsion it would be 45° (Beer et al. 2012). Additionally, mid-shaft bending stresses were calculated as

$$\sigma_{\text{bending}} = \frac{|\sigma_{\max}| + |\sigma_{\min}|}{2}, \quad (1)$$

where $\sigma_{\max}$ is the maximum (tensile) stress at mid-shaft and $\sigma_{\min}$ is the minimum (compressive) stress at mid-shaft. This assumes that planar strain conditions were in place (Biewener 1992), which was revealed by inspection of normal stress contours to be approximately true.
3. *Muscular support parameters*, related to Question 3 posed in the Introduction: the abduction moments of muscles that are predominantly suited to conferring hip abduction (i.e., iliofemoralis externus), and the long-axis rotation moments of muscles that are predominantly suited to conferring hip long-axis rotation (i.e., iliotrochantericus caudalis and puboischiofemorales internus 1 et 2 in non-avian theropods; iliotrochanterici caudalis et

medialis in the chicken). By being normalized to the product of the model's body weight and hip height, these moments give a size-independent measure of how much 'effort' a muscle exerts to stabilize a joint in a given axis:

$$M^* = \frac{a \cdot F_{\max} \cdot r_i}{m \cdot g \cdot h}, \quad (2)$$

where a is the activation level of the muscle, from 0 (inactive) to 1 (maximally active), $F_{\max}$ is the maximum force capable of being produced (set at two body weights as per Part II), r_i is the muscle's moment arm about joint axis i, m is body mass, g is the acceleration due to gravity (9.81 m/s^2) and h is hip height. It is worth noting that this analysis carries the caveat of ignoring biarticular muscles (e.g., iliotibiales) and co-contraction between agonistic and antagonistic muscles.

Given the small sample size of species examined here (n = 3), any assessment of the evolution of biomechanically relevant parameters is necessary ~~a~~ coarse ~~one~~. Since the hindlimb anatomy of *Daspletosaurus* is close to that inferred for the ancestral state of Coelurosauria, its results may taken to be representative of the most recent common ancestor of it and '*Troodon*'; likewise, since the anatomy of the '*Troodon*' model is close to that inferred for the ancestral state of Paraves, its results may taken to be representative of the most recent common ancestor of it and the chicken. Thus, by mapping results towards the most recent common ancestor of successive clades, the changes observed between *Daspletosaurus*, '*Troodon*'and the chicken are taken to be a surrogate for the actual sequence (if not pattern) of evolution along the theropod stem lineage.

III.4 Results

A total of five different postures for *Daspletosaurus*, and six postures for '*Troodon*', were tested before no further correspondence between principal stress trajectories and cancellous bone architectural patterns was able to be achieved (Fig. 4A,B). In the *Daspletosaurus* model, going from the worst to best postures tested, the angular deviation between the minimum compressive stress ($\boldsymbol{\sigma}_3$) and the mean direction of the primary fabric orientation ($\mathbf{u}_1$) in the femoral head decreased from 15.6° to 7.3°, a 53% reduction; likewise, the angular deviation between $\boldsymbol{\sigma}_3$ and $\mathbf{u}_1$

in the medial femoral condyle decreased from 11.7° to 2.8°, a 76% reduction. In the '*Troodon*' model, going from the worst to best postures tested, the angular deviation between $\boldsymbol{\sigma}_3$ and $\mathbf{u}_1$ in the femoral head decreased from 23.8° to 3.9°, an 84% reduction; likewise, the angular deviation between $\boldsymbol{\sigma}_3$ and $\mathbf{u}_1$ in the medial femoral condyle decreased from 28.3° to 24.2°, a 14% reduction. The final solution postures for both species are illustrated in Fig. 4C–H. As with the results for the chicken model (Part II), only minimal correspondence between principal stress trajectories and cancellous bone architecture was able to be achieved in the distal tibiotarsus of either species. Little correspondence was also able to be achieved in the fibular crest of the *Daspletosaurus* model's tibia. Thus, the remainder of this section will focus on the more proximal parts of the hindlimb.

III.4.1 Daspletosaurus *results*

In the solution posture, the principal stress trajectories in the femur showed a high degree of correspondence with the observed cancellous bone architecture throughout the bone (Figs 4A, 5, 6). Strong correspondence between $\boldsymbol{\sigma}_3$ (compressive) and cancellous bone architecture occurred in the femoral head and both medial and lateral femoral condyles. This correspondence included that between the mean direction of $\boldsymbol{\sigma}_3$ and $\mathbf{u}_1$ (Figs 5G, 6I). Correspondence between the maximum principal stress ($\boldsymbol{\sigma}_1$, tensile) and cancellous bone architecture occurred in the distal half of the fourth trochanter. Additionally, three instances of a double-arcuate pattern occurred, formed by $\boldsymbol{\sigma}_1$ and $\boldsymbol{\sigma}_3$, largely in the coronal plane. These correlate to three similar such patterns observed in the cancellous bone architecture of tyrannosaurids: in the femoral head and proximal metaphysis, in the lesser trochanter, and in the anterior and posterior parts of the distal femur proximal to the condyles. The double-arcuate patterns of $\boldsymbol{\sigma}_1$ and $\boldsymbol{\sigma}_3$ sometimes also occurred in the results for other postures tested, but they were often less developed compared to the solution posture.

Strong correspondence between principal stress trajectories and cancellous bone architecture also occurred in the proximal tibia and fibula (Fig. 7). The trajectory of $\boldsymbol{\sigma}_3$ corresponded closely with the observed architectural patterns of both the medial and lateral condyles, including a more

lateral inclination in the lateral condyle. In the cnemial crest of the tibia, the trajectory of $\boldsymbol{\sigma}_1$ largely paralleled the margins of the crest, as observed for cancellous bone fabric. Good correspondence between $\boldsymbol{\sigma}_3$ and cancellous bone architectural patterns was also observed in the fibular head, particularly for in the medial aspect of the bone (Fig. 7K,L).

III.4.2 'Troodon' *results*

As with the *Daspletosaurus* model, in the solution posture identified for '*Troodon*', the principal stress trajectories in the femur generally showed strong correspondence to the observed cancellous bone architecture (Figs 4B, 8, 9). Correspondence with $\boldsymbol{\sigma}_3$ occurred in the femoral head, under the greater trochanter and in both medial and lateral condyles; correspondence with $\boldsymbol{\sigma}_1$ occurred in the lesser trochanter. The mean direction of $\boldsymbol{\sigma}_3$ in the femoral head showed strong correspondence to the mean direction of $\mathbf{u}_1$ (Fig. 8E). A decent amount of correspondence between $\boldsymbol{\sigma}_3$ and $\mathbf{u}_1$ also occurred in the medial femoral condyle, although the direction of $\boldsymbol{\sigma}_3$ was notably more posteriorly inclined than the mean direction of $\mathbf{u}_1$ (Fig. 9E), as occurred in the chicken model of Part II. Unlike the results for the *Daspletosaurus* model, no double-arcuate pattern of $\boldsymbol{\sigma}_1$ and $\boldsymbol{\sigma}_3$ was present in '*Troodon*'; instead, their trajectories tended to spiral about the bone's long axis, much like the stress results for the chicken model.

Good correspondence between principal stress trajectories and cancellous bone architecture also occurred in the proximal tibia and fibula (Fig. 10). In the medial and lateral condyles, $\boldsymbol{\sigma}_3$ corresponded closely with observed architectural patterns, possessing a gentle posterior inclination, with a slight lateral inclination under the lateral condyle. In the cnemial crest, the trajectory of $\boldsymbol{\sigma}_1$ largely paralleled the margins of the distal part of the crest. In the fibular head, the principal stress trajectories showed good overall correspondence to the observed architectural patterns (Fig. 10K–M). Greater correspondence occurred laterally with $\boldsymbol{\sigma}_1$, but some correspondence was also present in the medial side with $\boldsymbol{\sigma}_3$.

III.4.3 Hip articulation results

In both variations in hip articulation tested for the *Daspletosaurus* model, the resulting principal stress trajectories of the proximal femur showed poorer correspondence with observed cancellous bone architecture than that achieved with the initial solution posture (Fig. 11). In particular, $\boldsymbol{\sigma}_3$, was broadly directed towards the more cylindrical part of the femoral head, lateral to the apex, rather than towards the apex itself. Additionally, the anterior inclination of $\boldsymbol{\sigma}_3$ in the femoral head was greater in both variations than that in the originally identified solution posture, and was markedly greater than the anterior inclination of the mean direction of $\mathbf{u}_1$.

III.4.4 Cross-species comparisons of biomechanical parameters

In terms of posture, hip extension, hip adduction-abduction, hip long-axis rotation and knee flexion angles all changed in a gradual fashion progressing from *Daspletosaurus* to '*Troodon*' to the chicken (Fig. 12). The same pattern also occurred for the anterior location of the whole-body COM and the degree of crouch. Furthermore, the degree of crouch of the solution postures matched closely with empirical predictions based on total leg length (Fig. 12C). In terms of bone loading, all parameters also changed in a gradual fashion progressing from *Daspletosaurus* to the chicken (Fig. 13A,B). Thus, in *Daspletosaurus*, the femur was loaded predominantly in mediolateral bending, whereas in the chicken the femur was loaded predominantly in torsion, with ~~bending~~ predominantly ~~of an anteroposterior nature~~. In '*Troodon*', torsion was more prominent compared to *Daspletosaurus*, but bending still remained the dominant loading regime. As with the other parameters, muscular support also changed gradually progressing from *Daspletosaurus* to the chicken Fig. 13C,D). In *Daspletosaurus*, the normalized hip abductor moment was relatively high and the normalized hip medial rotator moment was relatively low, whereas the situation was reversed in the chicken.

III.5 Discussion

Having previously demonstrated the validity and potential utility of the 'reverse' application of the trajectorial theory (Part II; Bishop et al. in review-b), the aim of the present study was to apply this approach to two extinct, non-avian theropods, *Daspletosaurus torosus* and '*Troodon*' (Troodontidae sp.), to gain new insight into their hindlimb locomotor biomechanics. In addition to deriving a 'characteristic posture' for both species, quantitative results were produced that have bearing on various questions concerning theropod locomotor biomechanics and its evolution, posed in Section III.2. In particular, the evolutionary-biomechanical hypotheses of Carrano (1998) and Hutchinson & Gatesy (2000) were able to be quantitatively tested in a novel way.

III.5.1 Postures

In the 'characteristic posture' identified for both non-avian theropods, there was generally a strong alignment between calculated principal stress trajectories and observed patterns in cancellous bone architecture, across the femur, proximal tibia and proximal fibula. It is important to note that this should not be presumed to be *the* posture used by these extinct species at any particular point in the stance phase; rather, the posture identified here is a time- and load-averaged characterization of the kinds of postures experienced on a daily basis. Nevertheless, since the posture previously identified for the chicken corresponds well to the posture of a typical avian hindlimb at around mid-stance in terrestrial locomotion (Part II), the postures derived for *Daspletosaurus* and '*Troodon*' are inferred to reflect the postures of these species at around the mid-stance of normal locomotion. Thus, *Daspletosaurus* is inferred to have stood and moved with a largely upright posture with a subvertical femoral orientation, whilst the limb posture of '*Troodon*' is inferred to have been more crouched, although not to the degree observed in extant birds. It is worth noting that the femoral orientation of the *Daspletosaurus* posture, in terms of the degree of hip extension, is very similar to that hypothesized for other large~~, basal~~ tetanuran species by previous workers such as *Tyrannosaurus* (Gatesy et al. 2009; Hutchinson 2004; Hutchinson et al. 2005), *Allosaurus* and *Acrocanthosaurus* (Bates et al. 2012). The inferences drawn in those studies were based on the posture that allowed for high locomotor forces to be sustained (Gatesy et al. 2009; Hutchinson 2004), or that achieved a maximal total moment arm of

644 the hip extensor muscles (Bates et al. 2012; Hutchinson et al. 2005). The rationale of the latter set
645 of studies is in some respects similar to the approach of the present study (which used static
646 optimization in the musculoskeletal modelling stage), in that both approaches are dependent on
647 the moment arms of individual muscles (see Part II, section II.5.1).
648
649
650 ***III.5.2 Articulation of the non-avian theropod hip joint***
651
652 The results of the exploratory analysis of hip articulations in the *Daspletosaurus* model supported
653 the inference made in Part I of this series: in non-avian theropods such as *Allosaurus* and
654 tyrannosaurids, the immediate articulation between the femur and acetabulum may have been
655 centred about the apex of the femoral head. Other articulations, involving greater contribution
656 from the cylindrical part of the femoral head lateral to the apex, did not result in as strong
657 correspondence between principal stresses and cancellous bone architecture. This is not to say
658 that these other articulations were not used during daily activity, rather that they may have been
659 used less frequently. Indeed, as the entire proximal surface of the non-avian theropod femur
660 typically bears a smooth, wrinkled texture indicative of a hyaline cartilage covering (Tsai &
661 Holliday 2015), this suggests that articulation between the lateral proximal femur and the
662 incipient antitrochanter on the ilium would have occurred on occasion, but the relatively
663 frequency of this remains unknown (see also Kambic et al. 2014; Kambic et al. 2015). This
664 interpretation of hip articulation is also consonant with anatomical considerations of the non-
665 avian theropod pelvis and sacrum. Specifically, a more lateral articulation of the (non-abducted)
666 femur with the acetabulum places the femoral head more medially with respect to the pelvis,
667 which could bring it into contact with the centra of the sacral vertebrae (e.g., Gilmore 1920;
668 Osborn 1917; Rauhut & Carrano 2016).
669
670 Combined with the results of the exploratory analysis, the solution posture identified for the
671 *Daspletosaurus* model can help move toward resolving the question of how theropods with
672 proximomedially inclined femoral heads, such as tyrannosaurids and carcharodontosaurids, kept
673 their feet positioned close to the body midline, as indicated by fossil trackways (e.g., McCrea et
674 al. 2014). Previously, working on the assumption that the cylindrical part of the femoral head

articulated with the acetabulum, researchers had found that the femur inevitably becomes markedly abducted from the body midline. Without further speculation about joint articulations or the nature of the intervening soft tissues (cartilage, menisci) more distally in the limb, this leads to an unnaturally wide foot placement (e.g., Bates et al. 2012; Hutchinson et al. 2005; Hutchinson et al. 2007). Indeed, in the second variation of hip articulation tested for the *Daspletosaurus* model, mediolateral step width was almost 47% of hip height, more than three times the typical step width observed in theropods (Bishop et al. 2017). With the hip articulation occurring at the apex of the femoral head, however, this allows for significant joint movement in other directions besides abduction-adduction. In particular, the solution posture identified for the *Daspletosaurus* model had a modest amount of external long-axis rotation, but little abduction of the femur; in fact, the femur was adducted slightly. Moreover, the asymmetry of the distal femoral condyles leads to a gently skewed orientation of the knee flexion-extension axis in the coronal plane, such that the distal crus is angled in towards the body midline (see Part II and Figs 1E and 2E). The combination of these features allows the pes to be positioned close to the midline, yet the upper limb be kept clear of the pelvis.

Despite the potential that this new interpretation may have for understanding how non-avian theropod hips may have articulated, it is worth emphasizing that it is based on a single posture, which at best can only be regarded as a snap shot of the limb during the stance phase of locomotion. A great deal more work is required if an understanding of dynamic joint articulations throughout the stride is to be achieved. One potential avenue is by using forward dynamic simulations (e.g., Sellers et al. 2017) to generate a variety of postures throughout the stance that may be used to inform musculoskeletal and finite element models. This would require more complex modelling of some joints than is currently done (e.g., three degrees of freedom for the hip), and would in turn require substantially greater computational power.

III.5.3 Theropod locomotor evolution

A second major objective of the current study was to test evolutionary-biomechanical hypotheses concerning posture, bone loading mechanics and muscular control strategies in theropods. In

doing so, insight would be gained as to how such aspects of theropod locomotion may have evolved on the line to birds. The results for the three theropod species modelled here demonstrate that, progressing through theropod phylogeny towards more derived species, the following trends occurred:

1. The whole-body COM moved anteriorly; this was to be expected, given that model mass properties were largely derived from models developed in the study of Allen et al. (2013), who showed the same pattern.
2. Hindlimb posture became more crouched, at least as far as the hip and knee joints are concerned. This is consonant with the findings of previous work (Carrano 1998; Gatesy 1990; Gatesy 1991).
3. Torsion became more prevalent than bending as the dominant loading regime of the femur.
4. The direction of bending of the femur changed from being predominantly mediolateral to being predominantly anteroposterior.
5. Hip abduction became overtaken by hip long-axis rotation as the main muscular control mechanism of stance-limb support.

For a given parameter, the value for '*Troodon*' was intermediate between that for *Daspletosaurus* and that for the chicken. This supports the hypothesis of a gradual evolutionary change in locomotor biomechanics along the line to birds, but more taxa from different parts of theropod phylogeny would need to be modelled to definitively rule out punctuated change at any point along the stem lineage. Regardless of the mode of evolution of these parameters, the above results do suggest that hindlimb posture, bone loading mechanics and muscular support strategies were tightly associated with each other, supporting the hypotheses of Carrano (1998) and Hutchinson & Gatesy (2000). Future development of models for other non-avian theropod species will help further test this interpretation.

The above trends identified in the present study parallel trends in other biomechanically relevant aspects, as noted by previous studies. These other trends include:

1. Modifications of pelvic and hindlimb osteology and musculature (Carrano 2000; Hutchinson 2001a; Hutchinson 2001b; Hutchinson 2002).
2. Decrease in tail length and prominence of caudofemoralis musculature (Gatesy 1990; Gatesy 1995; Gatesy 2002; Pittman et al. 2013).

3. A shift from caudofemoralis-mediated, hip-based limb retraction to 'hamstring'-mediated, knee-based limb retraction during gait (Gatesy 1990; Gatesy 1995; Gatesy 2002).
4. Changes in gross limb proportions, in particular a decrease in relative femur length, which in turn leads to an apparent increase in femoral diaphyseal robusticity (Carrano 1998; Gatesy & Middleton 1997).
5. The acquisition of a more continuous locomotor repertoire, where walking and running are not discrete gaits (Bishop et al. 2017).

The timing of some of these changes remains uncertain (see also Hutchinson 2006), but it appears that all were underway prior to the origin of Paraves (i.e., birds and their closest maniraptoran relatives such as '*Troodon*'), and that many, if not all, took place over a protracted period of time.

Most of the above changes also occurred in tandem with a progressive (Lee et al. 2014) or multi-step (Benson et al. in press) reduction in body size along the theropod stem lineage. A decrease in body size – either along the theropod stem lineage, or by directly comparing *Daspletosaurus*, '*Troodon*' and the chicken – might be expected in and of itself to bring about changes in posture, since posture correlates with body size in extant parasagittal tetrapods (Biewener 1989; Biewener 1990; Bishop et al. in review-a; Gatesy & Biewener 1991). However, since many other aspects of theropod anatomy and locomotor biomechanics also change in tandem with body size along the theropod stem lineage, it is presently not possible to disentangle the relative importance of body size (or any other single feature) on posture. That many aspects of theropod locomotor anatomy and biomechanics appear to have co-evolved over a protracted period of time, along with additional features such as forelimb enlargement (Dececchi & Larsson 2013) and elaboration of forelimb integument (Xu et al. 2014; Zelenitsky et al. 2012), is an interesting phenomenon that warrants further investigation.

The results of this study may also have more general implications for understanding locomotor biomechanics (and its evolution) in tetrapod species that employ a largely parasagittal stance and gait. Previous *in vivo* strain gauge studies of parasagittal mammals that use a more crouched femoral posture have shown that the femur experiences a sizeable amount of torsional loading, in addition to bending (Butcher et al. 2011; Keller & Spengler 1989). Additionally, finite element simulations of sit-to-stand and stand-to-sit behaviour in humans, behaviours that require limb

support during crouched femoral orientations, have revealed a marked increase in torsional loading of the femur compared to normal locomotion (Villette 2016). In concert with the results of this study, these observations suggest that there is a continuum in musculoskeletal mechanics spanning from crouched to upright postures, of which birds and humans are 'end members'. In upright postures, hip abduction is the dominant mode of limb support, which results in bending being the dominant mode of loading of the femur. However, as the femur becomes more crouched, the efficacy of hip abduction in providing limb support decreases, whilst that of hip long-axis rotation increases; this in turn loads the femur in a greater degree of torsion (see also Butcher et al. 2011).

III.5.4 Methodological considerations

A number of methodological considerations should be borne in mind when interpreting the results of the present study. None are considered to be of any major importance for the main interpretations made here, but they do highlight areas where future research efforts could be focused, potentially yielding further insight into theropod hindlimb biomechanics.

III.5.4.1 Correspondence in the distal tibiotarsus

It is worth re-iterating that little correspondence ~~was able to be achieved~~ between principal stresses and cancellous bone architecture in the distal parts of the tibiotarsus or fibula, in any posture tested for all three theropod species modelled. Additionally, the architectural patterns observed in the fibular crest of tyrannosaurid tibiae could not be replicated in the *Daspletosaurus* model. As discussed in Part II, this could reflect an inadequate modelling formulation, adaptation of these parts of the bones to many varied loading regimes, or a combination of both (or other) factors. Despite this, the architecture of cancellous bone in the distal tibiotarsus of theropods shows some strikingly different patterns between the various theropod groups. From a phenomenological perspective at least, this is indicative of marked differences in bone loading regimes, and by extension locomotor behaviour. It is therefore worthy of future modelling effort

to establish a more mechanistic link between cancellous bone architecture and musculoskeletal loading mechanics in this part of the hindlimb.

III.5.4.2 Pelvic orientation

One aspect of theropod posture that was not investigated in this study was the orientation of the pelvis. In all simulations, the pelvis of the three theropod species modelled was oriented similarly, with the sacral vertebrate oriented approximately horizontally and parallel to the *x*-axis of the global coordinate system. However, it is known that extant birds can employ significant amounts of pitch, roll or yaw during locomotion (Abourachid et al. 2011; Gatesy 1999a; Rubenson et al. 2007). If the pelvis underwent side-to-side rolling during locomotion in non-avian theropods, even by a small amount, this may have served to clear the pelvis and trunk further out of the way of the thigh of the stance leg. The effect of this would have been most obvious in species with well-developed pubic boots, such as large tyrannosaurids and allosauroids. Future investigation could therefore be directed towards incorporating one or more degrees of freedom in the pelvis segment of the models, as well incorporating additional degrees of freedom in other joints (e.g., knee) too. Caution would need to be exercised, however, as the number of variable parameters could quickly grow to be very large, which may require a great deal more iterations be tested before a 'solution posture' is satisfactorily obtained.

III.5.4.3 Stresses in the medial femoral condyle

As noted in the results of this study, as well as those of Part II, the mean direction of the minimum principal stress ($\boldsymbol{\sigma}_3$) in the medial femoral condyle was notably more posteriorly inclined than the mean direction of the primary fabric orientation of cancellous bone ($\mathbf{u}_1$), in both the chicken and '*Troodon*' models. This was the case regardless of the posture tested. The cause

for this discrepancy is probably twofold. Firstly, taking the mean direction of $\mathbf{u}_1$ in the medial condyle will average out the 'fan' of individual fabric vectors (see Part I) that is ubiquitous in theropods. Thus, there will be some parts of the condyle for which a greater correspondence between fabric direction and the calculated principal stresses will indeed occur, namely, where the fabric vectors are more posteriorly inclined than the overall orientation.

Secondly, it is quite possible that the individual $\mathbf{u}_1$ vectors throughout the medial condyle may also 'reflect' the maximum principal stress ($\boldsymbol{\sigma}_1$) in addition to $\boldsymbol{\sigma}_3$, and so do not fully align with the calculated directions of either one. Given that motion of the theropod knee is inferred to have predominantly occurred in the flexion-extension plane (but see Kambic et al. 2015), the main loading regimes expected in the femoral condyles would be expected be anteroposteriorly oriented, as also suggested by the 'butterfly pattern' of the secondary fabric direction in the condyles (see Part I). Hence, both $\boldsymbol{\sigma}_1$ and $\boldsymbol{\sigma}_3$ could be expected to be largely constrained to a parasagittal orientation, which could influence the direction of $\mathbf{u}_1$ throughout the medial condyle.

III.6 Conclusion

By applying the trajectorial theory in reverse, this study sought to identify a single, characteristic posture for two extinct, non-avian theropods that can explain a considerable amount of the architecture of cancellous bone observed in the hindlimb bones of these species. The postures derived for *Daspletosaurus torosus* and '*Troodon*' are inferred to reflect the postures used at around mid-stance during normal terrestrial locomotion, but should not be presumed to have been *the* postures used. The largely upright posture identified for *Daspletosaurus* is comparable to the postures previously hypothesized for other large, ~~basal~~ tetanuran species of non-avian theropod. The posture identified for '*Troodon*' is more crouched than that of *Daspletosaurus*, especially in regard to femoral orientation, but not to the degree observed in extant birds. The results of this study also provide an alternative perspective on the manner of articulation of the non-avian theropod hip joint, and suggest a solution to how non-avian theropods with proximomedially inclined femoral heads maintained narrow mediolateral foot placements.

In addition to improving understanding of posture in non-avian theropods, this study provides a new approach for how evolutionary-biomechanical hypotheses of locomotion can be explicitly and quantitatively tested. By using a previously underexplored line of evidence, cancellous bone architecture, the results of this study have supported the hypotheses of Carrano (1998) and Hutchinson & Gatesy (2000). Progressing from basal tetanurans and coelurosaurs through to extant birds, a number of important changes are inferred to have occurred in concert with one another, involving whole-body COM position, hindlimb posture, bone loading mechanics and muscular control strategies. The pattern of the changes also supports a more gradual fashion of change (as opposed to more punctuated), adding to the growing body of evidence suggesting that the unique locomotor repertoire of extant birds was acquired over a long period of time. However, only three species were modelled here, and so a more rigorous testing of the exact mode and tempo of evolutionary change awaits the modelling of additional species.

The integrative biomechanical modelling approach developed in Part II provides useful insights into non-avian theropod hindlimb locomotor biomechanics, as well as how this evolved along the line to extant birds. The generality of the approach means that it could be useful for understanding locomotor behaviour, and its evolution, in other extinct vertebrate groups as well. Examples of future research that could apply the approach include: forelimb posture and use in quadrupedal dinosaurs, such as ceratopsians (Fujiwara & Hutchinson 2012; Johnson & Ostrom 1995); the evolution of powered flight in birds, bats and pterosaurs (Bishop 2008; Heers & Dial 2012; Thewissen & Babcock 1992; Unwin 2005); the evolution of posture in synapsids on the line to mammals (Blob 2001; Kemp 1982); and the evolution of terrestrial locomotor capabilities in stem tetrapods (Clack 2012; Pierce et al. 2013). It may also prove to be of use for questions of biomechanics not related to locomotion, such as the posture of sauropod dinosaur necks (Stevens & Parrish 2005; Taylor et al. 2009).

III.7 Acknowledgements

The staff of the Geosciences Program of the Queensland Museum is thanked for the provision of workspace and access to literature: A. Rozefelds, K. Spring, R. Lawrence, P. Tierney, J. Wilkinson and D. Lewis. Much appreciation is extended to the staff and associated colleagues of the institutions that provided access to the material studied here: D. Henderson, B. Strlisky, G.

Housego, R. Russel, T. Courtenay, B. Sanchez and F. Therrien (Royal Tyrell Museum of Palaeontology, Drumheller); R. Irmis, C. Levitt-Bussian, C. Webb and P. Policelli (Natural History Museum of Utah, Salt Lake City); J. Horner, J. Scannella, D. Varricchio, D. Strosnider, C. Woodruff, D. Fowler and T. Carr (Museum of the Rockies, Bozeman). Many of the above people also provided helpful discussion on various aspects of theropod biology, and also helped transport specimens for CT scanning. Those who facilitated or performed the scanning itself are also greatly thanked: S. Purdy and D. Wetter (Canada Diagnostic Centres, Calgary); K. Ugrin and D. Van Why (Bozeman Deaconess Hospital, Bozeman); and S. Merchant, E. Hsu and J. Morgan (HSC Cores Research Facility, University of Utah, Salt Lake City). All scripts and data used are held in the Geosciences Collection of the Queensland Museum, and will be made available upon request to the Collections Manager.

III.8 References

Abourachid A, Hackert R, Herbin M, Libourel PA, Lambert F, Gioanni H, Provini P, Blazevic P, and Hugel V. 2011. Bird terrestrial locomotion as revealed by 3-D kinematics. *Zoology* 114:360–368.

Alexander RM. 1989. *Dynamics of Dinosaurs and Other Extinct Giants*. New York: Columbia University Press.

Allen V, Bates KT, Li Z, and Hutchinson JR. 2013. Linking the evolution of body shape and locomotor biomechanics in bird-line archosaurs. *Nature* 497:104–107.

Allen V, Paxton H, and Hutchinson JR. 2009. Variation in Center of Mass Estimates for Extant Sauropsids and its Importance for Reconstructing Inertial Properties of Extinct Archosaurs. *The Anatomical Record* 292:1442-1461.

Allmendinger RW, Cardozo NC, and Fisher D. 2013. *Structural Geology Algorithms: Vectors and Tensors*. Cambridge: Cambridge University Press.

Attene M, and Falcidieno B. 2006. ReMESH: An Interactive Environment to Edit and Repair Triangle Meshes. Proceedings of the Eighth International Conference on Shape Modeling and Applications. Matushima. p 271-276.

Bakker RT. 1986. *The Dinosaur Heresies*. New York: William Morrow & Company, Inc.

Bates BT, and Schachner ER. 2012. Disparity and convergence in bipedal archosaur locomotion. *Journal of the Royal Society Interface* 9:1339-1353.

Bates KT, Benson RBJ, and Falkingham PL. 2012. A computational analysis of locomotor anatomy and body mass evolution in Allosauroidea (Dinosauria: Theropoda). *Paleobiology* 38:486-507.

Bates KT, Falkingham PL, Breithaupt BH, Hodgetts D, Sellers WI, and Manning PL. 2009a. How big was 'Big Al'? Quantifying the effect of soft tissue and osteological unknowns on

mass predictions for *Allosaurus* (Dinosauria: Theropoda). *Palaeontologia Electronica* 12:14A.
Bates KT, Manning PL, Hodgetts D, and Sellers WI. 2009b. Estimating Mass Properties of Dinosaurs Using Laser Imaging and 3D Computer Modelling. *PLoS ONE* 4:e4532.
Beer FP, Johnston ER, Jr, DeWolf JT, and Mazurek DF. 2012. *Mechanics of Materials*. New York: McGraw-Hill.
Benson RBJ, Hunt G, Carrano MT, and Campione NE. in press. Cope's Rule and the adaptive landscape of dinosaur body size evolution. *Palaeontology*.
Biewener AA. 1989. Scaling Body Support in Mammals: Limb Posture and Muscle Mechanics. *Science* 245:45-48.
Biewener AA. 1990. Biomechanics of Mammalian Terrestrial Locomotion. *Science* 250:1097-1103.
Biewener AA. 1992. *In vivo* measurement of bone strain and tendon force. In: Biewener AA, ed. *Biomechanics – Structures and Systems: A Practical Approach*. New York: Oxford University Press.
Bishop KL. 2008. The evolution of flight in bats: narrowing the field of plausible hypotheses. *Quarterly Review of Biology* 83:153-169.
Bishop PJ, Clemente CJ, Graham DF, Lamas LP, Hutchinson JR, Rubenson J, Hancock JA, Wilson RS, Hocknull SA, Barrett RS, and Lloyd DG. in review-a. The Influence of Speed and Size on Avian Terrestrial Locomotor Biomechanics: Predicting Locomotion in Extinct Theropod Dinosaurs. *PLoS ONE*.
Bishop PJ, Clemente CJ, Weems RE, Graham DF, Lamas LP, Hutchinson JR, Rubenson J, Wilson RS, Hocknull SA, Barrett RS, and Lloyd DG. 2017. Using step width to compare locomotor biomechanics between extinct, non-avian theropod dinosaurs and modern obligate bipeds. *Journal of the Royal Society Interface* 14:20170276.
Bishop PJ, Hocknull SA, Clemente CJ, Hutchinson JR, Barrett RS, and Lloyd DG. in review-b. Cancellous bone architecture and theropod dinosaur locomotion. Part II – A new approach to reconstructing posture and locomotor biomechanics in extinct tetrapod vertebrates. *PeerJ*.
Bishop PJ, Hocknull SA, Clemente CJ, Hutchinson JR, Farke AA, Beck BR, Barrett RS, and Lloyd DG. in review-c. Cancellous bone architecture and theropod dinosaur locomotion. Part I – An examination of cancellous bone architecture in the hindlimb bones of theropods. *PeerJ*.
Blob RW. 2001. Evolution of hindlimb posture in nonmammalian therapsids: biomechanical tests of paleontological hypotheses. *Paleobiology* 27:14-38.
Brochu CA. 2003. Osteology of *Tyrannosaurus rex*: insights from a nearly complete skeleton and high-resolution computed tomographic analysis of the skull. *Society of Vertebrate Paleontology Memoir* 7:1-138.
Brusatte SL, Norell MA, Carr TD, Erickson GM, Hutchinson JR, Balanoff AM, Bever GS, Choiniere JN, Makovicky PJ, and Xu X. 2010. Tyrannosaur Paleobiology: New Research on Ancient Exemplar Organisms. *Science* 329:1481-1485.
Butcher MT, White BJ, Hudzik NB, Gosnell WC, Parrish JHA, and Blob RW. 2011. *In vivo* strains in the femur of the Virginia opossum (*Didelphis viginiana*) during terrestrial locomotion: testing hypotheses of evolutionary shifts in mammalian bone loading and design. *Journal of Experimental Biology* 214:2631-2640.

975 Campione NE, Evans DC, Brown CM, and Carrano MT. 2014. Body mass estimation in non-
976 avian bipeds using a theoretical conversion to quadruped stylopodial proportions.
977 *Methods in Ecology and Evolution* 5:913-923.
978 Cardozo NC, and Allmendinger RW. 2013. Spherical projections with OSXStereonet.
979 *Computers & Geosciences* 51:193-205.
980 Carrano MT. 1998. Locomotion in non-avian dinosaurs: integrating data from hindlimb
981 kinematics, in vivo strains, and bone morphology. *Paleobiology* 24:450-469.
982 Carrano MT. 2000. Homoplasy and the evolution of dinosaur locomotion. *Paleobiology* 26:489-
983 512.
984 Carrano MT. 2001. Implications of limb bone scaling, curvature and eccentricity in mammals
985 and non-avian dinosaurs. *Journal of Zoology* 254:41-55.
986 Carrano MT, and Hutchinson JR. 2002. Pelvic and hindlimb musculature of *Tyrannosaurus rex*
987 (Dinosauria: Theropoda). *Journal of Morphology* 253:207-228.
988 Christiansen P. 1998. Strength indicator values of theropod long bones, with comments on limb
989 proportions and cursorial potential. *Gaia* 15:241-255.
990 Christiansen P. 1999. Long bone scaling and limb posture in non-avian theropods: evidence for
991 differential allometry. *Journal of Vertebrate Paleontology* 19:666-680.
992 Clack JA. 2012. *Gaining Ground: The Origin and Evolution of Tetrapods*. Bloomington: Indiana
993 University Press.
994 Dececchi TA, and Larsson HCE. 2013. Body and limb size dissociation at the origin of birds:
995 uncoupling allometric constraints across a macroevolutionary transition. *Evolution*
996 67:2741-2752.
997 Delp SL, Anderson FC, Arnold AS, Loan P, Habib A, John CT, Guendelman E, and Thelen DG.
998 2007. OpenSim: Open-Source Software to Create and Analyze Dynamic Simulations of
999 Movement. *IEEE Transactions of Biomedical Engineering* 54:1940-1950.
1000 Farlow JO, Chapman RE, Breithaupt BH, and Matthews N. 2012. The Scientific Study of
1001 Dinosaur Footprints. In: Brett-Surman MK, Holtz TR, Jr, and Farlow JO, eds. *The*
1002 *Complete Dinosaur*. 2 ed. Bloomington: Indiana University Press, 712–759.
1003 Farlow JO, Smith MB, and Robinson JM. 1995. Body mass, bone "strength indicator," and
1004 cursorial potential of *Tyrannosaurus rex*. *Journal of Vertebrate Paleontology* 15:713-
1005 725.
1006 Fujiwara S, and Hutchinson JR. 2012. Elbow joint aductor moment arm as an indicator of
1007 forelimb posture in extinct quadrupedal tetrapods. *Proceedings of the Royal Society of*
1008 *London, Series B* 279:2561-2570.
1009 Gao C, Morschhauser EM, Varricchio DJ, Liu J, and Zhao B. 2012. A Second Soundly Sleeping
1010 Dragon: New Anatomical Details of the Chinese Troodontid *Mei long* with Implications
1011 for Phylogeny and Taphonomy. *PLoS ONE* 7:e45203.
1012 Gatesy SM. 1990. Caudofemoral musculature and the evolution of theropod locomotion.
1013 *Paleobiology* 16:170-186.
1014 Gatesy SM. 1991. Hind Limb Scaling in Birds and Other Theropods: Implications for Terrestrial
1015 Locomotion. *Journal of Morphology* 209:83-96.
1016 Gatesy SM. 1994. Neuromuscular Diversity in Archosaur Deep Dorsal Thigh Muscles. *Brain,*
1017 *Behavior and Evolution* 43:1-14.
1018 Gatesy SM. 1995. Functional evolution of the hindlimb and tail from basal theropods to birds. In:
1019 Thomason JJ, ed. *Functional Morphology in Vertebrate Paleontology*. New York:
1020 Cambridge University Press, 219–234.

1021 Gatesy SM. 1997. An Electromyographic Analysis of Hindlimb Function in *Alligator* During
1022 Terrestrial Locomotion. *Journal of Morphology* 234:197-212.
1023 Gatesy SM. 1999a. Guineafowl Hindlimb Function I: Cineradiographic Analysis and Speed
1024 Effects. *Journal of Morphology* 240:115–125.
1025 Gatesy SM. 1999b. Guineafowl Hindlimb Function II: Electromyographic Analysis and Motor
1026 Pattern Evolution. *Journal of Morphology* 240:127–142.
1027 Gatesy SM. 2002. Locomotor Evolution on the Line to Modern Birds. In: Chiappe LM, and
1028 Witmer LM, eds. *Mesozoic Birds: Above the Heads of the Dinosaurs*. Berkeley:
1029 University of California Press, 432–447.
1030 Gatesy SM, Bäker M, and Hutchinson JR. 2009. Constraint-based exclusion of limb poses for
1031 reconstructing theropod dinosaur locomotion. *Journal of Vertebrate Paleontology*
1032 29:535-544.
1033 Gatesy SM, and Biewener AA. 1991. Bipedal locomotion: effects of speed, size and limb posture
1034 in birds and humans. *Journal of Zoology* 224:127-147.
1035 Gatesy SM, and Middleton KM. 1997. Bipedalism, flight, and the evolution of theropod
1036 locomotor diversity. *Journal of Vertebrate Paleontology* 17:308-329.
1037 Gatesy SM, Middleton KM, Jenkins FA, Jr, and Shubin NH. 1999. Three-dimensional
1038 preservation of foot movements in Triassic theropod dinosaurs. *Nature* 399:141-144.
1039 Gilmore CW. 1920. Osteology of the carnivorous Dinosauria in the United States National
1040 Museum, with special reference to the genera *Antrodemus* (*Allosaurus*) and
1041 *Ceratosaurus*. *Bulletin of the United States National Museum* 110:1-159.
1042 Heers AM, and Dial KP. 2012. From extant to extinct: locomotor ontogeny and the evolution of
1043 avian flight. *Trends in Ecology and Evolution* 27:296-305.
1044 Henderson DM. 1999. Estimating the masses and centers of mass of extinct animals by 3-D
1045 mathematical slicing. *Paleobiology* 25:88-106.
1046 Henderson DM, and Snively E. 2003. *Tyrannosaurus* en pointe: allometry minimized rotational
1047 inertia of large carnivorous dinosaurs. *Biology Letters* 271:S57-S60.
1048 Horner JR, and Lessem D. 1993. *The Complete T. rex*. New York: Simon and Schuster, Inc.
1049 Hotton NH, III. 1980. An Alternative to Dinosaur Endothermy: The Happy Wanderers. In:
1050 Thomas RDK, and Olson EC, eds. *A Cold Look at the Warm-Blooded Dinosaurs*.
1051 Boulder: Westview Press, Inc., 311-350.
1052 Hutchinson JR. 2001a. The evolution of femoral osteology and soft tissues on the line to extant
1053 birds (Neornithes). *Zoological Journal of the Linnean Society* 131:169-197.
1054 Hutchinson JR. 2001b. The evolution of pelvic osteology and soft tissues on the line to extant
1055 birds (Neornithes). *Zoological Journal of the Linnean Society* 131:123-168.
1056 Hutchinson JR. 2002. The evolution of hindlimb tendons and muscles on the line to crown-group
1057 birds. *Comparative Biochemistry and Physiology, Part A* 133:1051-1086.
1058 Hutchinson JR. 2004. Biomechanical Modeling and Sensitivity Analysis of Bipedal Running
1059 Ability. II. Extinct Taxa. *Journal of Morphology* 262:441-461.
1060 Hutchinson JR. 2006. The evolution of locomotion in archosaurs. *Comptes Rendus Palevol*
1061 5:519-530.
1062 Hutchinson JR, and Allen V. 2009. The evolutionary continuum of limb function from early
1063 theropods to birds. *Naturwissenschaften* 96:423-448.
1064 Hutchinson JR, Anderson FC, Blemker SS, and Delp SL. 2005. Analysis of hindlimb muscle
1065 moment arms in *Tyrannosaurus rex* using a three-dimensional musculoskeletal computer
1066 model: implications for stance, gait, and speed. *Paleobiology* 31:676-701.

Hutchinson JR, Bates KT, Molnar J, Allen V, and Makovicky PJ. 2011. A Computational Analysis of Limb and Body Dimensions in Tyrannosaurus rex with Implications for Locomotion, Ontogeny and Growth. *PLoS ONE* 6:e26037.

Hutchinson JR, and Garcia M. 2002. *Tyrannosaurus* was not a fast runner. *Nature* 415:1018-1021.

Hutchinson JR, and Gatesy SM. 2000. Adductors, abductors, and the evolution of archosaur locomotion. *Paleobiology* 26:734-751.

Hutchinson JR, and Gatesy SM. 2006. Dinosaur locomotion: Beyond the bones. *Nature* 440:292-294.

Hutchinson JR, Miller CE, Fritsch G, and Hildebrandt T. 2008. The Anatomical Foundation for Multidisciplinary Studies of Animal Limb Function: Examples from Dinosaur and Elephant Limb Imaging Studies. In: Endo H, and Frey R, eds. *Anatomical Imaging: Towards a New Morphology*. Tokyo: Springer, 23-38.

Hutchinson JR, Ng-Thow-Hing V, and Anderson FC. 2007. A 3D interactive method for estimating body segmental parameters in animals: Application to the turning and running performance of *Tyrannosaurus rex*. *Journal of Theoretical Biology* 246:660-6800.

Jacobson RD, and Hollyday M. 1982. A Behavioural and Electromyographic Study of Walking in the Chick. *Journal of Neurophysiology* 48:238-256.

Johnson RE, and Ostrom JH. 1995. The forelimb of *Torosaurus* and an analysis of the posture and gait of ceratopsian dinosaurs. In: Thomason JJ, ed. *Functional Morphology in Vertebrate Paleontology*. Cambridge: Cambridge University Press, 205-218.

Kambic RE, Roberts TJ, and Gatesy SM. 2014. Long-axis rotation: a missing degree of freedom in avian bipedal locomotion. *Journal of Experimental Biology* 217:2770-2782.

Kambic RE, Roberts TJ, and Gatesy SM. 2015. Guineafowl with a twist: asymmetric limb control in steady bipedal locomotion. *Journal of Experimental Biology* 218:3836-3844.

Keller TS, and Spengler DM. 1989. Regulation of bone stress and strain in the immature and mature rat femur. *Journal of Biomechanics* 22:1115-1127.

Kemp TS. 1982. *Mammal-like Reptiles and the Origin of Mammals*. London: Academic Press.

Lambe LM. 1917. The Cretaceous theropodous dinosaur Gorgosaurus. *Memoirs of the Geological Survey of Canada* 100:1-84.

Lautenschlager S. 2016. Reconstructing the past: methods and techniques for the digital restoration of fossils. *Royal Society Open Science* 3:160342.

Lee MSY, Cau A, Naish D, and Dyke GJ. 2014. Sustained miniaturization and anatomical innovation in the dinosaurian ancestors of birds. *Science* 345:562-566.

Marsh RL, Ellerby DJ, Carr JA, Henry HT, and Buchanan CI. 2004. Partitioning the Energetics of Walking and Running: Swinging the Limbs is Expensive. *Science* 303:80-83.

Martelli S, Taddei F, Testi D, Delp SL, and Viceconti M. 2011. NMSBuilder: an application to personalize NMS models. Proceedings of the 23rd Congress of the International Society of Biomechanics. Brussels.

McCrea RT, Buckley LG, Farlow JO, Lockley MG, Currie PJ, Matthews NA, and Pemberton SG. 2014. A 'Terror of Tyrannosaurs': The First Trackways of Tyrannosaurids and Evidence of Gregariousness and Pathology in Tyrannosauridae. *PLoS ONE* 9:e103613.

Molnar RE, and Farlow JO. 1990. Carnosaur Paleobiology. In: Weishampel DB, Dodson P, and Osmólska H, eds. *The Dinosauria*. 1 ed. Berkeley: University of California Press, 210–224.

1112 Norell MA, and Makovicky PJ. 1997. Important Features of the Dromaeosaur Skeleton:
1113 Information from a New Specimen. *American Museum Novitates* 3215:1-28.
1114 Norell MA, and Makovicky PJ. 1999. Important Features of the Dromaeosaurid Skeleton II:
1115 Information from Newly Collected Specimens of *Velociraptor mongoliensis*. *American*
1116 *Museum Novitates* 3282:1-45.
1117 Osborn HF. 1917. Skeletal adaptations of *Ornitholestes*, *Struthiomimus*, *Tyrannosaurus*. *Bulletin*
1118 *of the American Museum of Natural History* 35:733-771.
1119 Ostrom JH. 1969. Osteology of *Deinonychus antirrhopus*, and unusual theropod from the Lower
1120 Cretaceous of Montana. *Bulletin of the Peabody Museum of Natural History* 30:1-165.
1121 Paul GS. 1998. Limb design, function and running performance in ostrich-mimics and
1122 tyrannosaurs. *Gaia* 15:257-270.
1123 Pauwels F. 1980. *Biomechanics of the Locomotor Apparatus*. Berlin: Springer-Verlag.
1124 Pierce SE, Hutchinson JR, and Clack JA. 2013. Historical Perspectives on the Evolution of
1125 Tetrapodomorph Movement. *Integrative and Comparative Biology* 53:209-223.
1126 Pittman M, Gatesy SM, Upchurch P, Goswani A, and Hutchinson JR. 2013. Shake a Tail
1127 Feather: The Evolution of the Theropod Tail into a Stiff Aerodynamic Surface. *PLoS*
1128 *ONE* 8:e63115.
1129 Rauhut OWM, and Carrano MT. 2016. The theropod dinosaur *Elaphrosaurus bambergi*
1130 Janensch, 1920, from the Late Jurassic of Tendaguru, Tanzania. *Zoological Journal of the*
1131 *Linnean Society* 178:546-610.
1132 Reilly SM, and Blob RW. 2003. Motor control of locomotor hindlimb posture in the American
1133 alligator (*Alligator mississippiensis*). *Journal of Experimental Biology* 206:4327-4340.
1134 Roberts TJ, Chen MS, and Taylor CR. 1998. Energetics of bipedal running. II. Limb design and
1135 running mechanics. *Journal of Experimental Biology* 205:2753-2762.
1136 Rubenson J, Lloyd DG, Besier TF, Heliams DB, and Fournier PA. 2007. Running in ostriches
1137 (*Stuthio camelus*): three-dimensional joint axes alignment and joint kinematics. *Journal*
1138 *of Experimental Biology* 210:2548-2562.
1139 Sellers WI, and Manning PL. 2007. Estimating dinosaur maximum running speeds using
1140 evolutionary robotics. *Proceedings of the Royal Society of London, Series B* 274:2711-
1141 2716.
1142 Sellers WI, Pond SB, Brassey CA, Manning PL, and Bates KT. 2017. Investigating the running
1143 abilities of *Tyrannosaurus rex* using stress-constrained multibody dynamic analysis.
1144 *PeerJ* 5:e3420.
1145 Stevens KA, and Parrish JM. 2005. Digital Reconstructions of Sauropod Dinosaurs and
1146 Implications for Feeding. In: Curry Rogers KA, and Wilson JA, eds. *The Sauropods:*
1147 *Evolution and Paleobiology*. Berkeley: University of California Press, 178-200.
1148 Taylor MP, Wedel MJ, and Naish D. 2009. Head and neck posture in sauropod dinosaurs
1149 inferred from extant animals. *Acta Palaeontologica Polonica* 54:213-220.
1150 Thewissen JGM, and Babcock SK. 1992. The Origin of Flight in Bats. *BioScience* 42:340-345.
1151 Thulborn T. 1990. *Dinosaur Tracks*. London: Chapman and Hall.
1152 Tsai HP, and Holliday CM. 2015. Articular Soft Tissue Anatomy of the Archosaur Hip Joint:
1153 Structural Homology and Functional Implications. *Journal of Morphology* 276:601-630.
1154 Tsuihiji T, Barsbold R, Watabe M, Tsogtbaatar K, Chinzorig T, Fujiyama Y, and Suzuki S.
1155 2014. An exquisitely preserved troodontid theropod with new information on the palatal
1156 structure from the Upper Cretaceous of Mongolia. *Naturwissenschaften* 101:131-142.
1157 Unwin DM. 2005. *The Pterosaurs: From Deep Time*. New York: Pi Press.

Valente G, Pitto L, Testi D, Seth A, Delp SL, Stagni R, Viceconti M, and Taddei F. 2014. Are Subject-Specific Musculoskeletal Models Robust to the Uncertainties in Parameter Identification? *PLoS ONE* 9:e112625.

van der Reest AJ, and Currie PJ. 2017. Troodontids (Theropoda) from the Dinosaur Park Formation, Alberta, with a description of a unique new taxon: implications for deinonychosaur diversity in North America. *Canadian Journal of Earth Sciences* 54:919-935.

Villette CC. 2016. Structural Meso and Microscale Finite Element Based Approaches for the prediction of Bone Architecture and Fracture PhD. Imperial College London.

Wall-Scheffler CM, Chumanov E, Steudel-Numbers K, and Heiderscheit B. 2010. Electromyography Activity Across Gait and Incline: The Impact of Muscular Activity on Human Morphology. *American Journal of Physical Anthropology* 143:601-611.

Xu X, Norell MA, Wang X, Makovicky PJ, and Wu X. 2002. A basal troodontid from the Early Cretaceous of China. *Nature* 415:780-784.

Xu X, Zhou Z, Dudley R, Mackem S, Chuong C-M, Erickson GM, and Varricchio DJ. 2014. An integrative approach to understanding bird origins. *Science* 346:1253293.

Zelenitsky DK, Therrien F, Erickson GM, DeBuhr CL, Kobayashi Y, Eberth DA, and Hadfield F. 2012. Feathered Non-Avian Dinosaurs from North America Provide Insight into Wing Origins. *Science* 338:510-514.

III.9 Figure captions

Figure 1. The musculoskeletal model of the *Daspletosaurus* hindlimb developed in this study. This is shown in the 'neutral posture' for all joints, that is, when all joint angles are zero. (A–C) Geometries of the musculotendon actuators in relation to the bones, in lateral (A), anterior (B) and oblique anterolateral (C) views. (D–F) Location and orientation of joint coordinate systems (red, green and blue axes), the centres of mass for each segment (grey and white balls) and the soft tissue volumes used to calculate mass properties; these are shown in the same views as A–C. Also reported in D are the masses for each segment. In D–F, the flexion-extension axis of each joint is the blue axis. For scale, the length of each arrow in the triad of the global coordinate system is 500 mm.

Figure 2. The musculoskeletal model of the '*Troodon*' hindlimb developed in this study. This is shown in the neutral posture for all joints. (A–C) Geometries of the musculotendon actuators in

relation to the bones, in lateral (A), anterior (B) and oblique anterolateral (C) views. (D–F) Location and orientation of joint coordinate systems (red, green and blue axes), the centres of mass for each segment (grey and white balls) and the soft tissue volumes used to calculate mass properties; these are shown in the same views as A–C. Also reported in D are the masses for each segment. In D–F, the flexion-extension axis of each joint is the blue axis. For scale, the length of each arrow in the triad of the global coordinate system is 200 mm.

Figure 3. Varying the articulation of the hip joint in the *Daspletosaurus* model. (A, B) The original 'solution posture' identified for the *Daspletosaurus* model. (C, D) The first variation in hip articulation, where the femur (and limb distal to it) is moved medially by 50 mm. (E, F) The second variation in hip articulation, where the femur (and limb distal to it) is moved medially by 50 mm, also with a sizeable amount of hip abduction and external long-axis rotation. A, C and E are in oblique anterolateral view; B, D and F are in anterior view. Intervening soft tissues used in the finite element simulations are shown in turquoise; for clarity, the ilium and pubis are shown translucent in B, D and F. Also illustrated in B are the relative diameters of the femoral head (solid lines) and the acetabulum (dashed lines).

Figure 4. The identified solution postures for *Daspletosaurus* and '*Troodon*'. (A, B) Calculated angular deviation between the minimum principal stress ($\boldsymbol{\sigma}_3$) and the mean direction of the primary fabric orientation ($\mathbf{u}_1$) in the femoral head (grey bars) and medial femoral condyle (white bars) for each posture tested, for *Daspletosaurus* (A) and '*Troodon*' (B). This shows the progressive improvement in alignment between stresses and cancellous bone architecture across the postures tested. (C–E) The solution posture for *Daspletosaurus* in lateral (C), dorsal (D) and anterior (E) views. (F–H) The solution posture for '*Troodon*' in lateral (F), dorsal (G) and anterior (H) views. Also illustrated in C and F are stick figure representations of the other postures tested, and the whole-body COM of the solution posture. The solution postures resulted in the greatest degree of overall correspondence between principal stress trajectories and observed cancellous bone architectural patterns, as assessed by qualitative comparisons across the

femur, tibiotarsus and fibula, as well as quantitative results for the femoral head and medial femoral condyle.

Figure 5. Principal stress trajectories for the proximal femur in the solution posture of *Daspletosaurus*, compared with observed cancellous bone fabric. For easier visual comparison, these stress trajectories were 'downsampled' in a custom MATLAB script, by interpolating the raw stress results at each finite element node to a regular grid. (A) Vector field of $\boldsymbol{\sigma}_1$ (red) and $\boldsymbol{\sigma}_3$ (blue) in a 3-D slice through the proximal femur, parallel to the coronal plane and through the middle of the femoral head, in anterior view. Note how the trajectory of $\boldsymbol{\sigma}_3$ projects towards the apex of the femoral head (green braces). (B) Geometric representation of cancellous bone architecture in the proximal femur of *Allosaurus* and tyrannosaurids (cf. Part I), in the same view as A. (C) Vector field of $\boldsymbol{\sigma}_1$ and $\boldsymbol{\sigma}_3$ in a 3-D slice through the lesser trochanter, parallel to the plane of the trochanter, in anterolateral view. (D) Geometric representation of cancellous bone architecture in the lesser trochanter of *Allosaurus* and tyrannosaurids (cf. Part I), in the same view as C. (E) Vector field of $\boldsymbol{\sigma}_3$ in the femoral head, shown as a 3-D slice parallel to the sagittal plane and through the apex of the head, in medial view. (F) Geometric representation of cancellous bone architecture in the femoral head of *Allosaurus* and tyrannosaurids (cf. Part I), in the same view as E. (G) Comparison of the mean direction of $\boldsymbol{\sigma}_3$ in the femoral head (blue) and the estimated mean direction of $\mathbf{u}_1$ for *Allosaurus* and tyrannosaurids (red), plotted on an equal-angle stereoplot with northern hemisphere projection (using StereoNet 9.5; Allmendinger et al. 2013; Cardozo & Allmendinger 2013). Inset shows location of region for which the mean direction of $\boldsymbol{\sigma}_3$ was calculated.

Figure 6. Principal stress trajectories for the distal femur and fourth trochanter in the solution posture of *Daspletosaurus*, compared with observed cancellous bone fabric. (A) Vector field of $\boldsymbol{\sigma}_1$ (red) and $\boldsymbol{\sigma}_3$ (blue) in a 3-D slice, parallel to the coronal plane and through the anterior aspect of the distal metaphysis, in anterior view. (B) Geometric representation of cancellous bone architecture in the distal metaphysis of *Allosaurus* and tyrannosaurids (cf. Part I), in the same view as A. (C) Vector field of $\boldsymbol{\sigma}_1$ in the fourth trochanter, in medial view. (D) Geometric

representation of cancellous bone architecture in the fourth trochanter of *Allosaurus* and tyrannosaurids (cf. Part I), in the same view as C. (E) Vector field of $\boldsymbol{\sigma}_3$ in the lateral condyle, shown as a 3-D slice parallel to the sagittal plane and through the middle of the condyle. (F) Geometric representation of cancellous bone architecture in the lateral condyle of *Allosaurus* and tyrannosaurids (cf. Part I), in the same view as E. (G) Vector field of $\boldsymbol{\sigma}_3$ in the medial condyle, shown as a 3-D slice parallel to the sagittal plane and through the middle of the condyle. (H) Geometric representation of cancellous bone architecture in the medial condyle of *Allosaurus* and tyrannosaurids (cf. Part I), in the same view as G. (I) Comparison of the mean direction of $\boldsymbol{\sigma}_3$ in the medial condyle (blue) and the estimated mean direction of $\mathbf{u}_1$ for *Allosaurus* and tyrannosaurids (red), plotted on an equal-angle stereoplot with southern hemisphere projection. Inset shows location of region for which the mean direction of $\boldsymbol{\sigma}_3$ was calculated.

Figure 7. Principal stress trajectories for the tibia and fibula in the solution posture for *Daspletosaurus*, compared with observed cancellous bone fabric. (A) Vector field of $\boldsymbol{\sigma}_3$ in the medial tibial condyle, shown as a 3-D slice through the middle of the condyle and parallel to the sagittal plane, in medial view. (B) Geometric representation of cancellous bone architecture in the medial tibial condyle of *Allosaurus* and tyrannosaurids (cf. Part I), in the same view as A. (C) Vector field of $\boldsymbol{\sigma}_3$ in the medial and lateral tibial condyles, shown as 3-D slices through the middle of the condyles and parallel to the coronal plane, in posterior view. (D) Geometric representation of cancellous bone architecture in the medial and lateral tibial condyles of *Allosaurus* and tyrannosaurids (cf. Part I), in the same view as C. (E) Vector field of $\boldsymbol{\sigma}_3$ in the lateral tibial condyle, shown as a 3-D slice through the middle of the condyle and parallel to the sagittal plane, in lateral view. (F) Geometric representation of cancellous bone architecture in the lateral tibial condyle of *Allosaurus* and tyrannosaurids (cf. Part I), in the same view as E. (G) Vector field of $\boldsymbol{\sigma}_1$ in the cnemial crest, shown as a 3-D slice parallel to the coronal plane, in anterior view. (H) Geometric representation of cancellous bone architecture in cnemial crest of *Allosaurus* and tyrannosaurids (cf. Part I), sectioned in the plane of the crest, shown in the same view as G; blue section lines illustrate primary architectural direction. (I) Vector field of $\boldsymbol{\sigma}_1$ in the cnemial crest, shown as a 3-D slice parallel to the sagittal plane, in medial view. (J) Geometric representation of cancellous bone architecture in cnemial crest of *Allosaurus* and tyrannosaurids

(cf. Part I), sectioned in the plane of the crest, shown in the same view as I. (K) Vector field of $\boldsymbol{\sigma}_3$ in the medial aspect of the fibular head, in medial view. (L) Geometric representation of cancellous bone architecture in the fibular head of *Allosaurus* and tyrannosaurids (cf. Part I), in the same view as K.

Figure 8. Principal stress trajectories for the proximal femur in the solution posture of '*Troodon*', compared with observed cancellous bone fabric. (A, B) Vector field of $\boldsymbol{\sigma}_3$ in the femoral head, shown as 3-D slices parallel to the coronal plane (A, in anterior view) and sagittal plane (B, in medial view). (C, D) Vector field of $\mathbf{u}_1$ in the femoral head, in the same views as A and B, respectively (cf. Part I). (E) Comparison of the mean direction of $\boldsymbol{\sigma}_3$ in the femoral head (blue) and the mean direction of $\mathbf{u}_1$ (red), plotted on an equal-angle stereoplot with northern hemisphere projection. Inset shows location of region for which the mean direction of $\boldsymbol{\sigma}_3$ was calculated. (F, G) Vector field of $\boldsymbol{\sigma}_3$ under the greater trochanter, shown as 3-D slices parallel to the coronal plane (F, in posterior view) and sagittal plane (G, in lateral view). (H, I) Vector field of u_1 under the greater trochanter, shown in the same views as F and G, respectively (cf. Part I). (J) Vector field of $\boldsymbol{\sigma}_1$ in the lesser trochanter, shown in oblique anterolateral view. (K) Vector field of $\mathbf{u}_1$ in the lesser trochanter, shown in the same view as J for both specimens studied (cf. Part I).

Figure 9. Principal stress trajectories for the distal femoral condyles in the solution posture of '*Troodon*', compared with observed cancellous bone fabric. (A) Vector field of $\boldsymbol{\sigma}_3$ in the lateral condyle, shown as a 3-D slice parallel to the sagittal plane. (B) Vector field of $\mathbf{u}_1$ in the lateral condyle, shown in the same view as A (cf. Part I). (C) Vector field of $\boldsymbol{\sigma}_3$ in the medial condyle, shown as a 3-D slice parallel to the sagittal plane. (D) Vector field of $\mathbf{u}_1$ in the medial condyle, shown in the same view as C (cf. Part I). (E) Comparison of the mean direction of $\boldsymbol{\sigma}_3$ in the medial condyle (blue) and the mean direction of $\mathbf{u}_1$ (red), plotted on an equal-angle stereoplot with southern hemisphere projection. This shows that in the solution posture the mean direction of $\boldsymbol{\sigma}_3$ was of the same general azimuth as the mean direction of $\mathbf{u}_1$, but was markedly more posteriorly inclined. Inset shows location of region for which the mean direction of $\boldsymbol{\sigma}_3$ was calculated.

Figure 10. Principal stress trajectories for the tibia and fibula in the solution posture for '*Troodon*', compared with observed cancellous bone fabric. (A) Vector field of $\boldsymbol{\sigma}_3$ in the medial tibial condyle, shown as a 3-D slice through the middle of the condyle and parallel to the sagittal plane, in medial view. (B) Vector field of $\mathbf{u}_1$ in the medial tibial condyle, in the same view as A (cf. Part I). (C) Vector field of $\boldsymbol{\sigma}_3$ in the medial and lateral tibial condyles, shown as 3-D slices through the middle of the condyles and parallel to the coronal plane, in posterior view. (D) Vector field of $\mathbf{u}_1$ in the medial and lateral tibial condyles, in the same view as C (cf. Part I). (E) Vector field of $\boldsymbol{\sigma}_3$ in the lateral tibial condyle, shown as a 3-D slice through the middle of the condyle and parallel to the sagittal plane, in lateral view. (F) Vector field of $\mathbf{u}_1$ in the lateral tibial condyle, in the same view as E (cf. Part I). (G) Vector field of $\boldsymbol{\sigma}_1$ in the cnemial crest, shown as a 3-D slice parallel to the coronal plane, in anterior view. (H) Vector field of $\mathbf{u}_1$ in the cnemial crest, in the same view as G (cf. Part I). (I) Vector field of $\boldsymbol{\sigma}_1$ in the cnemial crest, shown as a 3-D slice parallel to the sagittal plane, in medial view. (J) Vector field of $\mathbf{u}_1$ in the cnemial crest, in the same view as I (cf. Part I). (K) Vector field of $\boldsymbol{\sigma}_1$ in the lateral fibular head, in lateral view. (L) Vector field of $\boldsymbol{\sigma}_3$ in the medial fibular head, in medial view (reversed). (M) Vector field of $\mathbf{u}_1$ in the fibular head, in the same view as K (cf. Part I).

Figure 11. Principal stress trajectories for the proximal femur of *Daspletosaurus* in the two variations in hip articulation tested. (A) Vector field of $\boldsymbol{\sigma}_3$ in the first variation tested, shown as a 3-D slice parallel to the coronal plane and through the middle of the femoral head. (B) Vector field of $\boldsymbol{\sigma}_3$ in the first variation tested, shown as a 3-D slice parallel to the sagittal plane and through the apex of the femoral head. (C) Vector field of $\boldsymbol{\sigma}_3$ in the second variation tested, shown as a 3-D slice parallel to the coronal plane and through the middle of the femoral head. (D) Vector field of $\boldsymbol{\sigma}_3$ in the second variation tested, shown as a 3-D slice parallel to the sagittal plane and through the apex of the femoral head. A and C are in anterior view, B and D are in medial view. Note in particular how the trajectory of $\boldsymbol{\sigma}_3$ projects towards the more cylindrical part of the femoral head, lateral to the apex (green braces); compare to Fig. 5A,B,E,F. Also note in **C** how $\boldsymbol{\sigma}_3$ has a strong medial component near the apex of the head.

Figure 12. Comparison of parameters related to posture, extracted from the solution postures of the three species modelled: *Daspletosaurus* ('D'), '*Troodon*' ('T') and the chicken ('C'). (A) Schematic illustration of the solution postures retrieved for the three species, along with the location of the whole-body centre of mass (black and white disc). (B) Whole-body centre of mass location anterior to the hips, normalized to total leg length. (C) Degree of crouch for each species, both as measured from the solution posture, as well as empirically predicted from the data reported by Bishop et al. (in review-a). (D) Angles of the hip and knee joints. The hip extension angle is expressed relative to the horizontal, whereas the knee flexion angle is expressed relative to the femur. (E) Long-axis rotation and adduction-abduction of the hip joint. Positive values indicate external rotation and abduction (respectively), whereas negative values indicate internal rotation and adduction (respectively).

Figure 13. Comparison of parameters related to bone loading mechanics and muscular support, extracted from the solution postures of the three species modelled: *Daspletosaurus* ('D'), '*Troodon*' ('T') and the chicken ('C'). (A) Orientation of the neutral axis of bending and the orientation of principal stresses ($\boldsymbol{\sigma}_1$ and $\boldsymbol{\sigma}_3$) relative to the femur long-axis, both measured at mid-shaft. Insets show the neutral axis with respect to the mid-shaft cross-section, as well as anatomical directions (A, anterior; P, posterior; M, medial; L, lateral). (B) Ratio of maximum shear to bending stress in the femoral mid-shaft. (C) Normallized moments of hip abductor and medial rotator muscles. The hip abductor for all species is the iliofemoralis externus (activation set to zero in the chicken; see Part II). In *Daspletosaurus* and '*Troodon*', the medial rotators are the iliotrochantericus caudalis and puboischiofemorales internus 1 et 2; in the chicken, they are the iliotrochanterici caudalis et medius. (D) Oblique anterolateral view of the hip of *Daspletosaurus*, showing the abductor and medial rotator muscles (colour codes as in C).

Table 1(on next page)

The specimens utilized in building the models of *Daspletosaurus torosus* and ‘ *Troodon* ’, as well as the settings used to acquire CT scans.

The geometry of specimens that were not CT scanned was captured via digital photogrammetry.

Table 1. The specimens utilized in building the models of *Daspletosaurus torosus* and '*Troodon*'. Also listed are the settings used in acquiring CT scans; the geometry of specimens that were not CT scanned was captured via digital photogrammetry.

Higher-order taxonomy	Species	Specimen number*	Element	CT scan settings					
				Machine	Peak tube voltage (kV)	Tube current (mA)	Exposure time (ms)	In-plane pixel resolution (mm)	Slice thickness (mm)
Coelurosauria, Tyrannosauridae	*Albertosaurus sarcophagus*	TMP 81.010.0001	Pubis						
Coelurosauria, Tyrannosauridae	*Albertosaurus sarcophagus*	TMP 81.010.0001	Ischium						
Coelurosauria, Tyrannosauridae	*Gorgosaurus libratus*	TMP 1994.012.0603	Metatarsals II–IV + distal tarsals	GE Lightspeed Ultra	140	150	1195	0.703	1.25
Coelurosauria, Tyrannosauridae	*Daspletosaurus torosus*	TMP 2001.036.0001	Femur	GE Lightspeed Ultra	140	150	1195	0.838	1.25
Coelurosauria, Tyrannosauridae	*Daspletosaurus torosus*	TMP 2001.036.0001	Tibia	GE Lightspeed Ultra	120	245	1195	0.832	1.25
Coelurosauria, Tyrannosauridae	*Daspletosaurus torosus*	TMP 2001.036.0001	Fibula	GE Lightspeed Ultra	120	245	1195	0.832	1.25
Coelurosauria, Tyrannosauridae	*Daspletosaurus torosus*	TMP 2001.036.0001	Astragalus	GE Lightspeed Ultra	140	155	1195	0.879	1.25
Coelurosauria, Tyrannosauridae	*Daspletosaurus torosus*	TMP 2001.036.0001	Metatarsal IV + lateral distal tarsal	GE Lightspeed Ultra	120	185	1195	0.738	1.25
Coelurosauria, Tyrannosauridae	*Daspletosaurus torosus*	TMP 2001.036.0001	Ilium						
Coelurosauria, Tyrannosauridae	*Daspletosaurus torosus*	TMP 2001.036.0001	Pubis						
Coelurosauria, Tyrannosauridae	*Daspletosaurus torosus*	TMP 2001.036.0001	Ischium						
Coelurosauria, Tyrannosauridae	*Tyrannosaurus rex*	MOR 009	Metatarsal V	Toshiba Aquilion 64	135	250	750	0.625	0.5
Coelurosauria, Tyrannosauridae	*Daspletosaurus horneri*	MOR 590	Metatarsals II–IV + phalanges						
Coelurosauria, Tyrannosauridae	*Tyrannosaurus rex*	MOR 980	Pubis						

Table 1 (continued).

Higher-order taxonomy	Species	Specimen number*	Element	CT scan settings					
				Machine	Peak tube voltage (kV)	Tube current (mA)	Exposure time (ms)	In-plane pixel resolution (mm)	Slice thickness (mm)
Coelurosauria, Tyrannosauridae	*Tyrannosaurus rex*	MOR 980	Ischium						
Coelurosauria, Tyrannosauridae	*Daspletosaurus horneri*	MOR 1130	Calcaneum	Toshiba Aquilion 64	135	150	1000	0.526	0.5
Coelurosauria, Tyrannosauridae	*Daspletosaurus horneri*	MOR 1130	Metatarsal I	Toshiba Aquilion 64	135	150	1000	0.526	0.5
Coelurosauria, Tyrannosauridae	*Teratophoneus curriei*	UMNH VP 16690	Pubis						
Coelurosauria, Tyrannosauridae	*Teratophoneus curriei*	UMNH VP 16690	Ischium						
Paraves, Troodontidae	*Latenivenatrix mcmasterae*	TMP 1992.036.0575	Metatarsals II–V	Siemens Inveon	80	250	1700	0.05	0.05
Paraves, Troodontidae	Troodontidae sp.	MOR 553l-7.27.8.67	Ischium						
Paraves, Troodontidae	Troodontidae sp.	MOR 553s-7.11.91.41	Tibia	Siemens Inveon	80	200	1900	0.04	0.04
Paraves, Troodontidae	Troodontidae sp.	MOR 553s-7.28.91.239	Femur	Siemens Inveon	80	200	1800	0.04	0.04
Paraves, Troodontidae	Troodontidae sp.	MOR 553s-8.3.9.387	Pubis						
Paraves, Troodontidae	Troodontidae sp.	MOR 553s-8.6.92.168	Metatarsal I						
Paraves, Troodontidae	Troodontidae sp.	MOR 553s-8.17.92.265	Fibula	Siemens Inveon	80	250	1600	0.04	0.04
Paraves, Troodontidae	Troodontidae sp.	MOR 748	Femur	Siemens Inveon	80	200	1900	0.04	0.04
Paraves, Troodontidae	Troodontidae sp.	MOR 748	Tibia + astragalus + calcaneum	Siemens Inveon	80	200	1900	0.04	0.04
Paraves, Troodontidae	Troodontidae sp.	MOR 748	Metatarsals II–IV	Siemens Inveon	80	200	1900	0.04	0.04
Paraves, Troodontidae	Troodontidae sp.	MOR 748	Ilium						
Paraves, Troodontidae	Troodontidae sp.	MOR uncatalogued	Ilium						

*Collection number abbreviations: MOR, Museum of the Rockies; TMP, Royal Tyrrell Museum of Palaeontology; UMNH VP; Natural History Museum of Utah.

Table 2(on next page)

The origins and insertions of each of the muscles and ligaments represented in the *Daspletosaurus* and '*Troodon*' musculoskeletal models.

Specific differences between the two theropods are noted where appropriate.

Table 2. The origins and insertions of each of the muscles and ligaments represented in the *Daspletosaurus* and '*Troodon*' musculoskeletal models. Specific differences between the two theropods are noted where appropriate.

Muscle or ligament	Abbreviation	Origin	Insertion
Iliotibialis 1	IT1	Anterior rim of lateral ilium	Cnemial crest
Iliotibialis 2	IT2	Dorsal rim of ilium, lateral surface	Cnemial crest
Iliotibialis 3	IT3	Dorsal rim of postacetabular ilium	Cnemial crest
Ambiens	AMB	Preacetabular process on proximal pubis	Cnemial crest
Femorotibialis externus	FMTE	Lateral femoral shaft	Cnemial crest
Femorotibialis internus	FMTI	Anteromedial femoral shaft	Cnemial crest
Iliofibularis	ILFB	Lateral postacetabular ilium, between IFE and FTE; posterior to median vertical ridge of the ilium in *Daspletosaurus*	Fibular tubercle
Iliofemoralis externus	IFE	Lateral ilium, anterodosal to acetabulum; anterior to median vertical ridge of the ilium in *Daspletosaurus*	Trochanteric shelf of femur
Iliotrochantericus caudalis	ITC	Lateral preacetabular ilium	Lesser trochanter
Puboischiofemoralis internus 1	PIFI1	Iliac preacetabular fossa; also descending onto lateral surface of pubic peduncle in *Daspletosaurus*	Anteromedial aspect of proximal femur
Puboischiofemoralis internus 2	PIFI2	Near PIFI1 origin, probably anterior to it (iliac preacetabular fossa)	Distal to lessor trochanter; on accessory trochanter in *Daspletosaurus*
Flexor tibialis internus 1	FTI1	Low tubercle on posterolateral ischial shaft in *Daspletosaurus*; distal end of ischium in '*Troodon*'	Medial proximal tibia
Flexor tibialis internus 3	FTI3	Ischial tuberosity on posterolateral proximal ischium in *Daspletosaurus*; proximal ischial shcaft in '*Troodon*'	Medial proximal tibia
Flexor tibialis externus	FTE	Lateral postacetabular ilium	Medial proximal tibia
Adductor femoris 1	ADD1	Lateral surface of obturator process	Medial posterodistal surface of femoral shaft; large scarred region in *Daspletosaurus*
Adductor femoris 2	ADD2	Posterodorsal rim of ischium	Lateral posterodistal surface of femoral shaft; large scarred region in *Daspletosaurus*
Puboischiofemoralis externus 1	PIFE1	Anterior surface of pubic apron	Greater trochanter
Puboischiofemoralis externus 2	PIFE2	Posterior surface of pubix apron	Greater trochanter
Puboischiofemoralis externus 3	PIFE3	Lateral ischium, between ADD1 and ADD2	Greater trochanter
Ischiotrochantericus	ISTR	Medial surface of ischium	Lateral proximal femur

Table 2 (continued).

Muscle or ligament	Abbreviation	Origin	Insertion
Caudofemoralis longus	CFL	Caudal vertebral centra, probably from caudal vertebrae 1–15 in *Daspletosaurus* and caudal vertebrae 1–10 in '*Troodon*'	Medial surface of fourth trochanter in *Daspletosaurus*, posteromedial surface of proximal femur in '*Troodon*'
Caudofemoralis brevis	CFB	Brevis fossa of ilium	Lateral surface of fourth trochanter in *Daspletosaurus*, posterolateral surface of proximal femur in '*Troodon*'
Gastrocnemius lateralis	GL	Posterolateral surface of distal femur	Posterior surface of metatarsals II-IV
Gastrocnemius medialis	GM	Medial proximal tibia	Posterior surface of metatarsals II-IV
Flexor digitorum longus	FDL	Posterior surface of distal femur	Ventral aspect of digit II-IV phalanges
Flexor digitorum brevis	FDB	Posterior surface of metatarsals II-IV	Ventral aspect of digit II-IV phalanges
Flexor hallucis longus	FHL	Posterior surface of femur	Ventral aspect of digit I phalanges
Extensor digitorum longus	EDL	Distal anterolateral femur; possibly also proximal anterior tibia in *Daspletosaurus*, and possibly also distal anterolateral femur in '*Troodon*'	Dorsal aspect of digit II-IV phalanges
Extensor digitorum brevis	EDB	Anterior surface of metatarsals	Dorsal aspect of digit II-IV phalanges
Extensor hallucis longus	EHL	Distal fibula	Dorsal aspect of digit I ungual
Tibialis anterior	TA	Anterior surface of proximal tibia	Anteroproximal metatarsals II-IV
Fibularis longus	FL	Anterolateral surface of tibia and/or fibula	Posterolateral ankle region (e.g., metatarsal V)
Fibularis brevis	FB	Distal to FL on fibula	Anterolateral ankle region (e.g., metatarsal IV)
Knee medial collateral ligament	KMCL	Depression on medial surface of medial femoral condyle	Medial proximal tibiotarsus, proximal to FCLP and FCM insertions
Knee lateral collateral ligament	KLCL	Lateral surface of lateral femoral condyle	Lateral fibular head
Ankle medial collateral ligament	AMCL	Depression on medial surface of astragalus	Medial proximal tarsometatarsus
Ankle lateral collateral ligament	ALCL	Depression on lateral surface of calcaneum	Lateral proximal tarsometatarsus

Table 3(on next page)

Hypothetical activities of the muscle actuators used in the *Daspletosaurus* and '*Troodon*' simulations.

X = active (capable of exerting up to two body weights of force), O = inactive (exerts zero force).

Table 3. Hypothetical activities of the muscle actuators used in the *Daspletosaurus* and '*Troodon*' simulations. X = active (capable of exerting up to two body weights of force), O = inactive (exerts zero force).

Muscle	Activity
IT1	X
IT2	X
IT3	X
AMB	X
FMTE	X
FMTI	X
ILFB	X
IFE	X
ITC	X
PIFI1	X
PIFI2	X
FTI1	X
FTI3	X
FTE	X
ADD1	X
ADD2	X
PIFE1	O
PIFE2	O
PIFE3	O
ISTR	X
CFL	X
CFB	X
GL	X
GM	X
FDL	X
FDB	X
FHL	X
EDL	O
EDB	O
EHL	O
TA	O
FL	O
FB	O

Figure 1(on next page)

The musculoskeletal model of the Daspletosaurus hindlimb developed in this study.

This is shown in the ‘neutral posture’ for all joints, that is, when all joint angles are zero. (A–C) Geometries of the musculotendon actuators in relation to the bones, in lateral (A), anterior (B) and oblique anterolateral (C) views. (D–F) Location and orientation of joint coordinate systems (red, green and blue axes), the centres of mass for each segment (grey and white balls) and the soft tissue volumes used to calculate mass properties; these are shown in the same views as A–C. Also reported in D are the masses for each segment. In D–F, the flexion-extension axis of each joint is the blue axis. For scale, the length of each arrow in the triad of the global coordinate system is 500 mm.

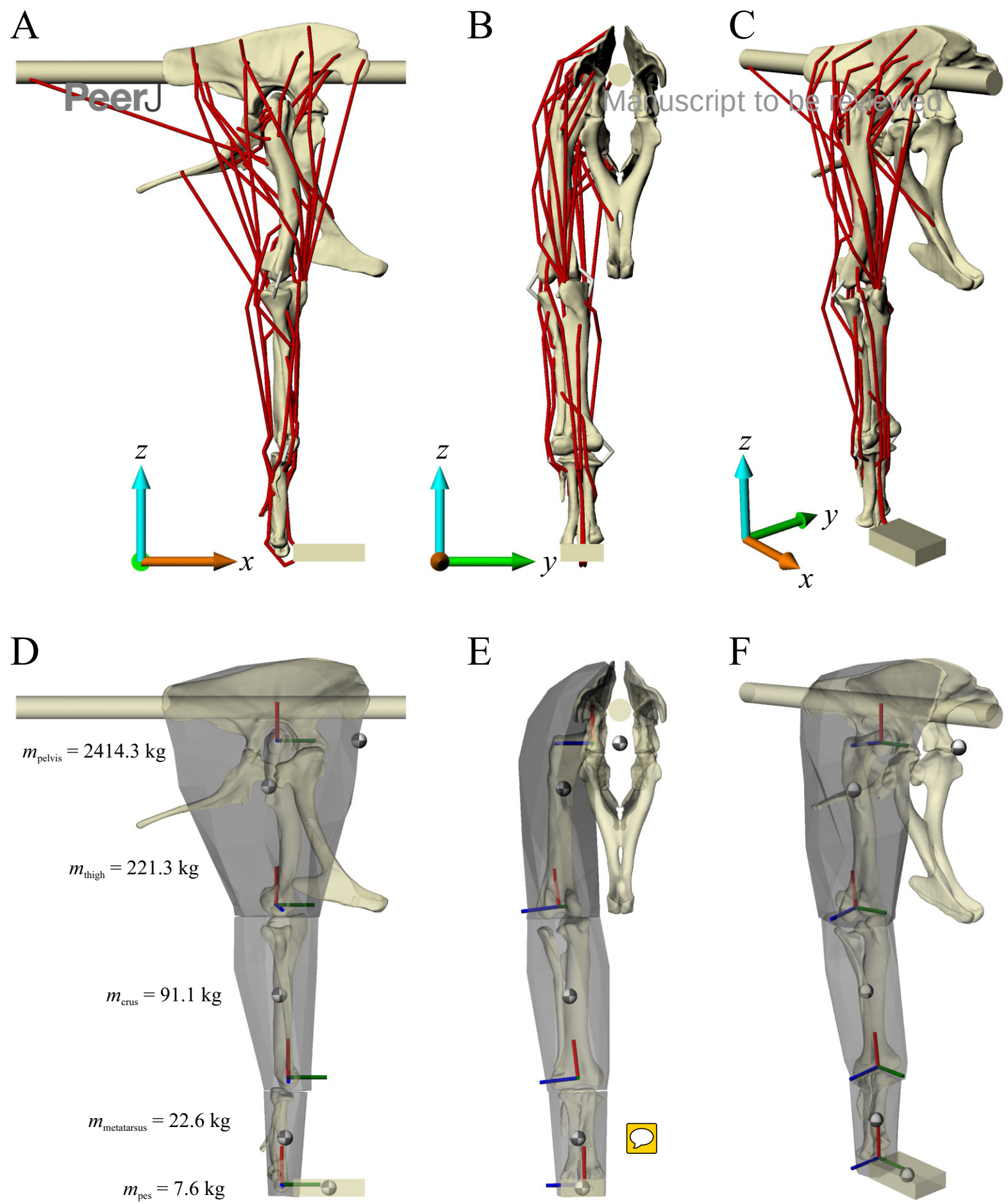

Figure 2(on next page)

The musculoskeletal model of the ‘ Troodon’ hindlimbdeveloped in this study.

This is shown in the neutral posture for all joints. (A–C) Geometries of the musculotendon actuators in relation to the bones, in lateral (A), anterior (B) and oblique anterolateral (C) views. (D–F) Location and orientation of joint coordinate systems (red, green and blue axes), the centres of mass for each segment (grey and white balls) and the soft tissue volumes used to calculate mass properties; these are shown in the same views as A–C. Also reported in D are the masses for each segment. In D–F, the flexion-extension axis of each joint is the blue axis. For scale, the length of each arrow in the triad of the global coordinate system is 200 mm.

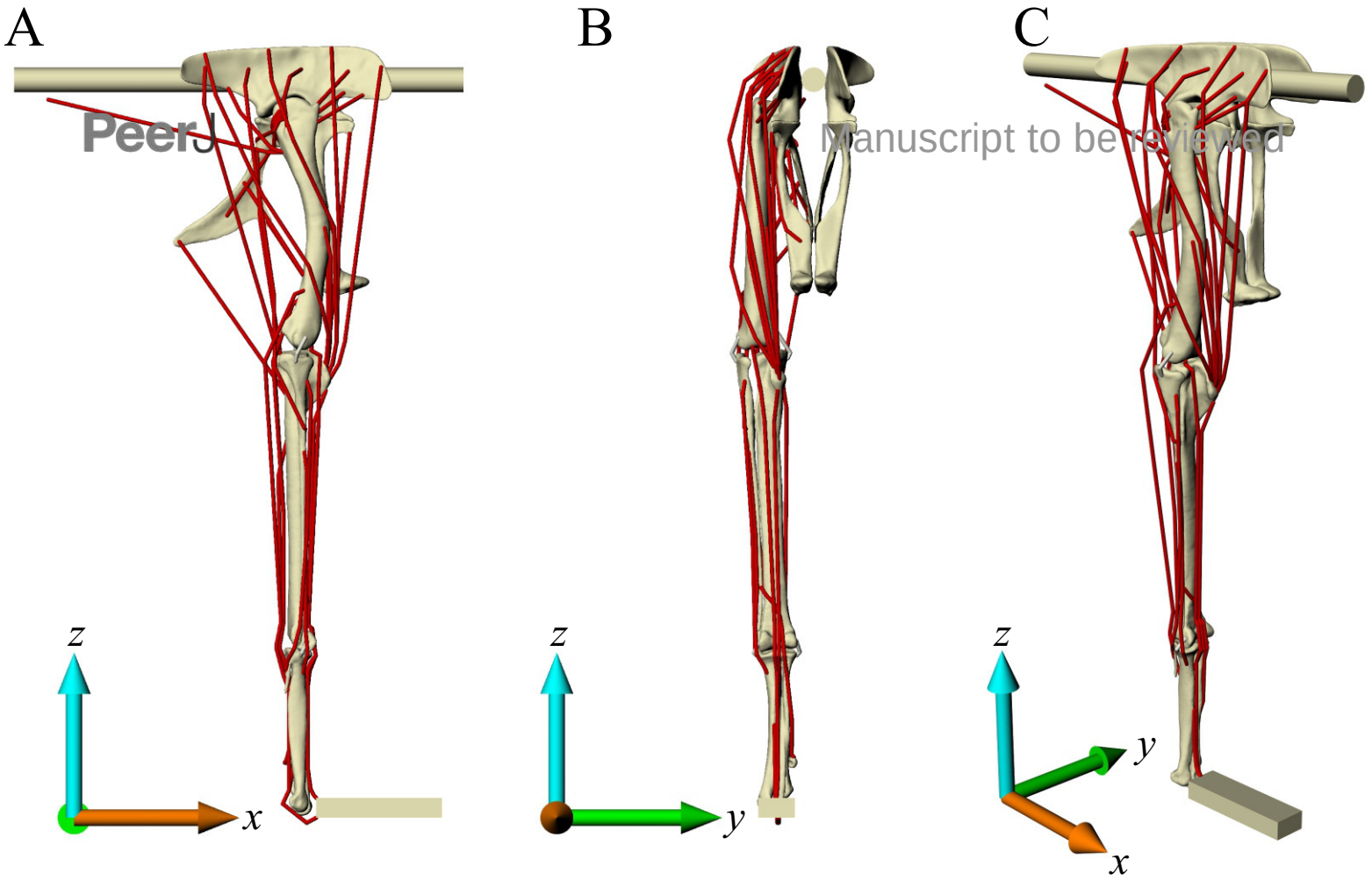

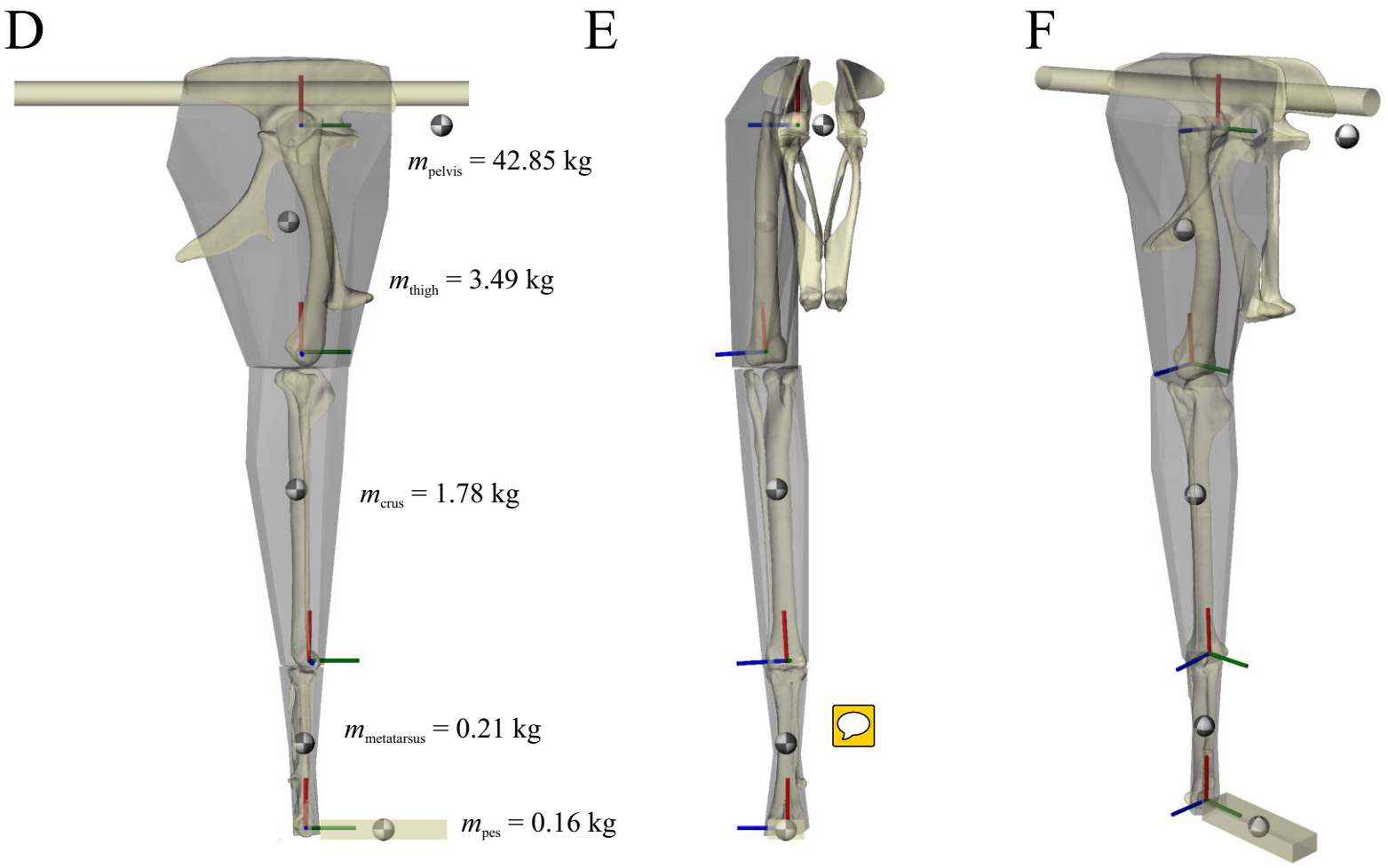

Figure 3(on next page)

Varying the articulation of the hip joint in the Daspletosaurus model.

(A, B) The original ‘solution posture’ identified for the Daspletosaurus model. (C, D) The first variation in hip articulation, where the femur (and limb distal to it) is moved medially by 50 mm. (E, F) The second variation in hip articulation, where the femur (and limb distal to it) is moved medially by 50 mm, also with a sizeable amount of hip abduction and external long-axis rotation. A, C and E are in oblique anterolateral view; B, D and F are in anterior view. Intervening soft tissues used in the finite element simulations are shown in turquoise; for clarity, the ilium and pubis are shown translucent in B, D and F. Also illustrated in B are the relative diameters of the femoral head (solid lines) and the acetabulum (dashed lines).

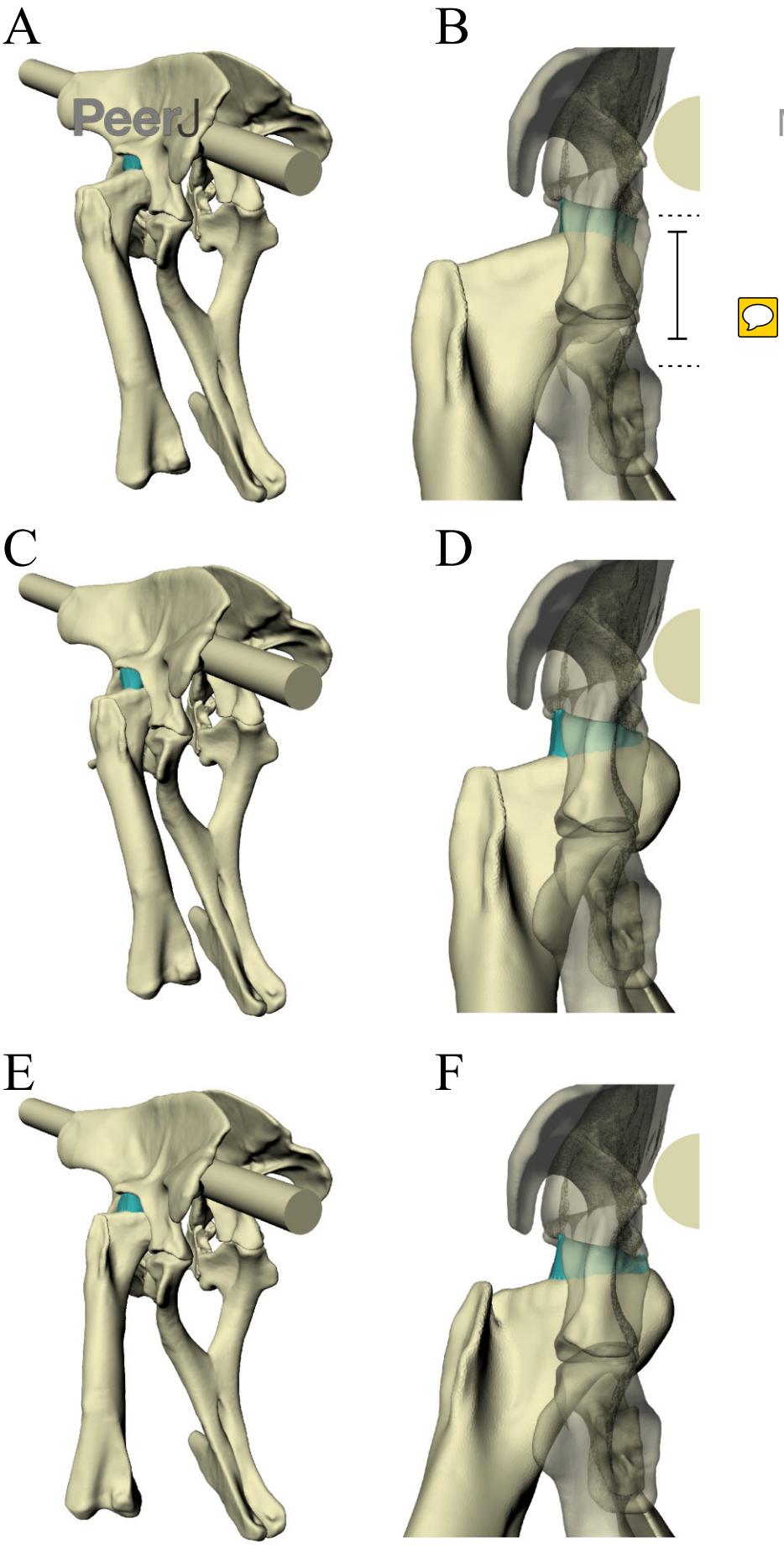

Figure 4(on next page)

The identified solution postures for Daspletosaurus and ‘ Troodon ’.

(A, B) Calculated angular deviation between the minimum principal stress ($\boldsymbol{\sigma}_3$) and the mean direction of the primary fabric orientation ($\mathbf{u}_1$) in the femoral head (grey bars) and medial femoral condyle (white bars) for each posture tested, for Daspletosaurus (A) and ‘ Troodon ’ (B). This shows the progressive improvement in alignment between stresses and cancellous bone architecture across the postures tested. (C–E) The solution posture for Daspletosaurus in lateral (C), dorsal (D) and anterior (E) views. (F–H) The solution posture for ‘ Troodon ’ in lateral (F), dorsal (G) and anterior (H) views. Also illustrated in C and F are stick figure representations of the other postures tested, and the whole-body COM of the solution posture. The solution postures resulted in the greatest degree of overall correspondence between principal stress trajectories and observed cancellous bone architectural patterns, as assessed by qualitative comparisons across the femur, tibiotarsus and fibula, as well as quantitative results for the femoral head and medial femoral condyle.

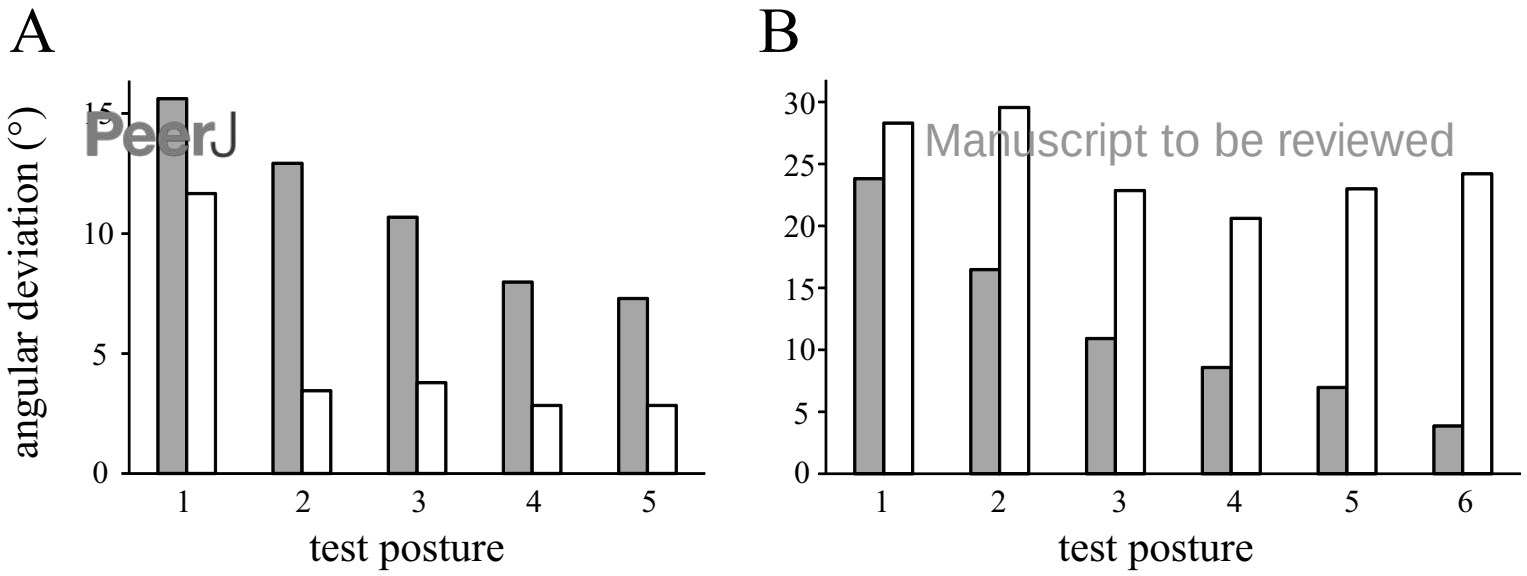

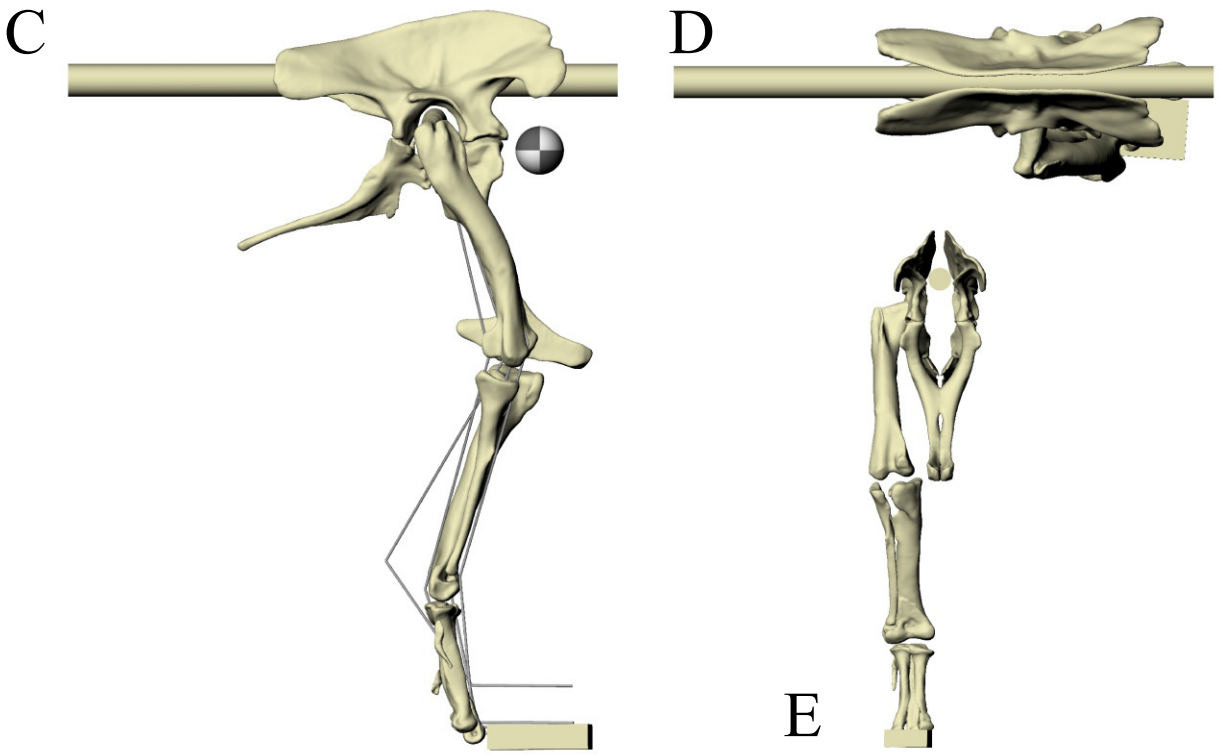

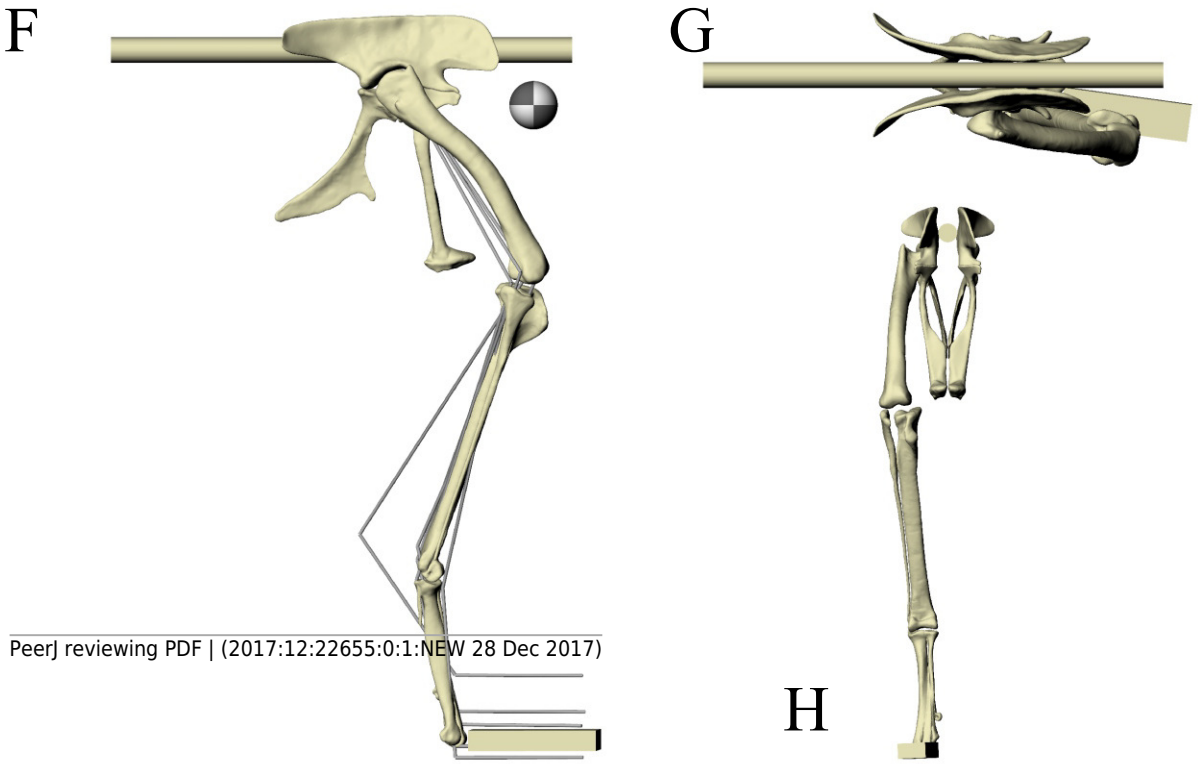

Figure 5(on next page)

Principal stress trajectories for the proximal femurin the solution posture of Daspletosaurus , compared with observed cancellousbone fabric.

For easier visual comparison, these stress trajectories were ‘downsampled’ in a custom MATLAB script, by interpolating the raw stress results at each finite element node to a regular grid. (A) Vector field of $\boldsymbol{\sigma}_1$ (red) and $\boldsymbol{\sigma}_3$ (blue) in a 3-D slice through the proximal femur, parallel to the coronal plane and through the middle of the femoral head, in anterior view. Note how the trajectory of $\boldsymbol{\sigma}_3$ projects towards the apex of the femoral head (green braces). (B) Geometric representation of cancellous bone architecture in the proximal femur of Allosaurus and tyrannosaurids (cf. Part I), in the same view as A. (C) Vector field of $\boldsymbol{\sigma}_1$ and $\boldsymbol{\sigma}_3$ in a 3-D slice through the lesser trochanter, parallel to the plane of the trochanter, in anterolateral view. (D) Geometric representation of cancellous bone architecture in the lesser trochanter of Allosaurus and tyrannosaurids (cf. Part I), in the same view as C. (E) Vector field of $\boldsymbol{\sigma}_3$ in the femoral head, shown as a 3-D slice parallel to the sagittal plane and through the apex of the head, in medial view. (F) Geometric representation of cancellous bone architecture in the femoral head of Allosaurus and tyrannosaurids (cf. Part I), in the same view as E. (G) C omparison of the mean direction of $\boldsymbol{\sigma}_3$ in the femoral head (blue) and the estimated mean direction of $\mathbf{u}_1$ for Allosaurus and tyrannosaurids (red), plotted on an equal-angle stereoplot with northern hemisphere projection (using StereoNet 9.5; Allmendinger et al. 2013; Cardozo & Allmendinger 2013) . Inset shows location of region for which the mean direction of $\boldsymbol{\sigma}_3$ was calculated.

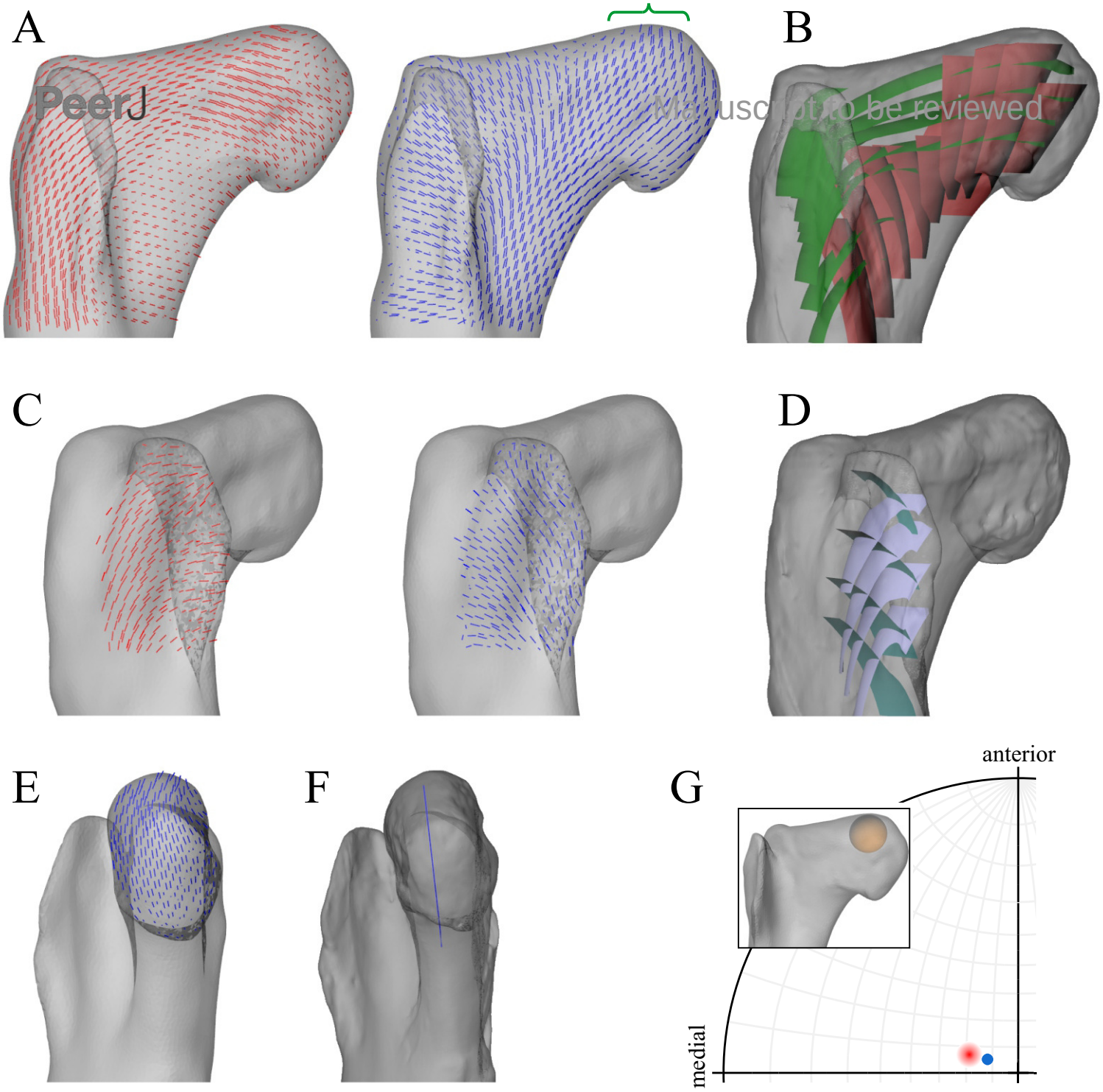

Figure 6(on next page)

Principal stress trajectories for the distal femur andfourth trochanter in the solution posture of Daspletosaurus , compared withobserved cancellous bone fabric.

(A) V ector field of $\boldsymbol{\sigma}_1$ (red) and $\boldsymbol{\sigma}_3$ (blue) in a 3-D slice, parallel to the coronal plane and through the anterior aspect of the distal metaphysis, in anterior view. (B) Geometric representation of cancellous bone architecture in the distal metaphysis of Allosaurus and tyrannosaurids (cf. Part I), in the same view as A. (C) Vector field of $\boldsymbol{\sigma}_1$ in the fourth trochanter, in medial view. (D) G eometric representation of cancellous bone architecture in the fourth trochanter of Allosaurus and tyrannosaurids (cf. Part I), in the same view as C. (E) Vector field of $\boldsymbol{\sigma}_3$ in the lateral condyle, shown as a 3-D slice parallel to the sagittal plane and through the middle of the condyle. (F) G eometric representation of cancellous bone architecture in the lateral condyle of Allosaurus and tyrannosaurids (cf. Part I), in the same view as E. (G) Vector field of $\boldsymbol{\sigma}_3$ in the medial condyle, shown as a 3-D slice parallel to the sagittal plane and through the middle of the condyle. (H) G eometric representation of cancellous bone architecture in the medial condyle of Allosaurus and tyrannosaurids (cf. Part I), in the same view as G. (I) C omparison of the mean direction of $\boldsymbol{\sigma}_3$ in the medial condyle (blue) and the estimated mean direction of $\mathbf{u}_1$ for Allosaurus and tyrannosaurids (red), plotted on an equal-angle stereoplot with southern hemisphere projection. Inset shows location of region for which the mean direction of $\boldsymbol{\sigma}_3$ was calculated.

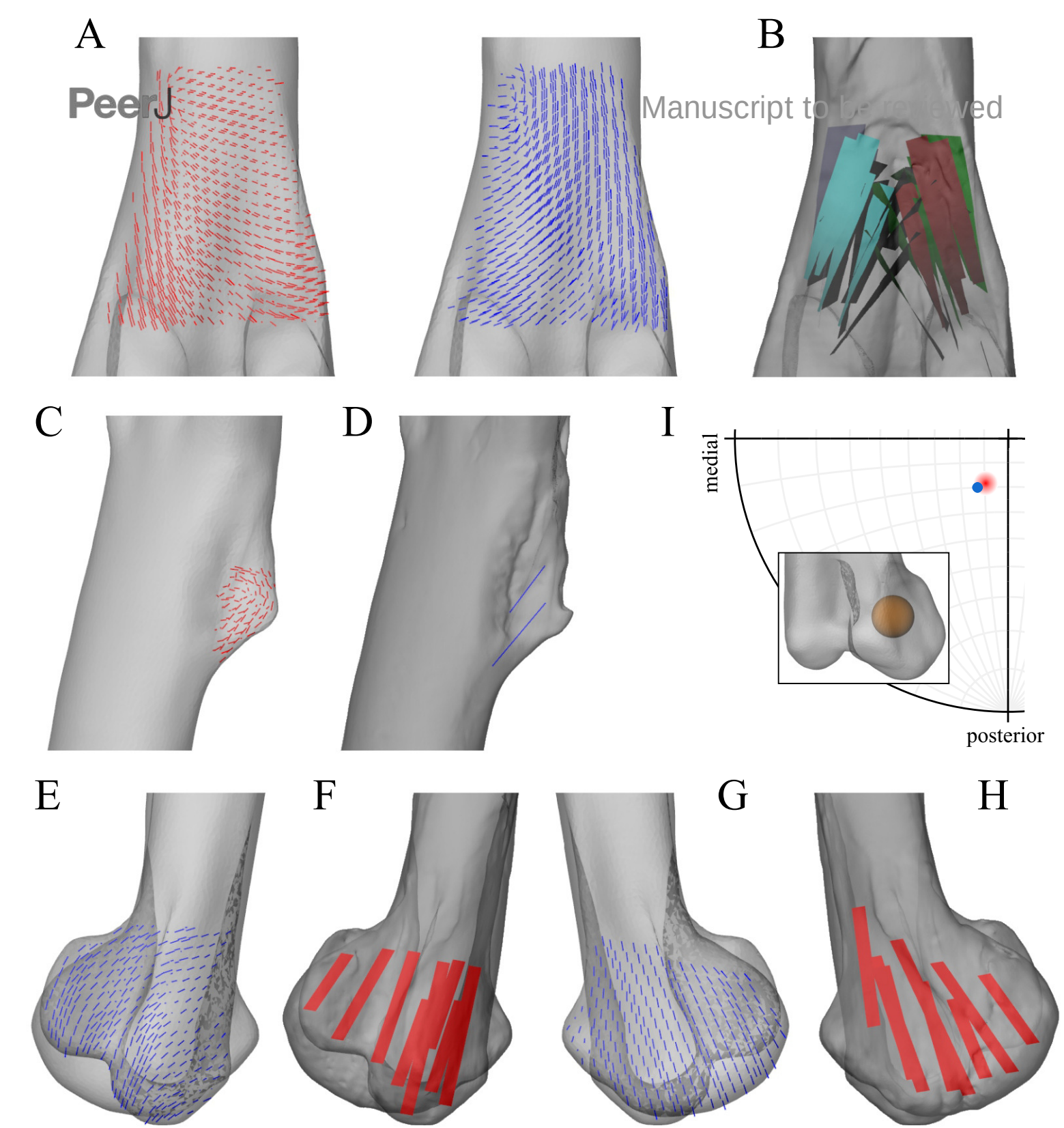

Figure 7 (on next page)

Principal stress trajectories for the tibia and fibulain the solution posture for Daspletosaurus , compared with observed cancellousbone fabric.

(A) Vector field of $\boldsymbol{\sigma}_3$ in the medial tibial condyle, shown as a 3-D slice through the middle of the condyle and parallel to the sagittal plane, in medial view. (B) G eometric representation of cancellous bone architecture in the medial tibial condyle of Allosaurus and tyrannosaurids (cf. Part I), in the same view as A. (C) Vector field of $\boldsymbol{\sigma}_3$ in the medial and lateral tibial condyles, shown as 3-D slices through the middle of the condyles and parallel to the coronal plane, in posterior view. (D) G eometric representation of cancellous bone architecture in the medial and lateral tibial condyles of Allosaurus and tyrannosaurids (cf. Part I), in the same view as C. (E) Vector field of $\boldsymbol{\sigma}_3$ in the lateral tibial condyle, shown as a 3-D slice through the middle of the condyle and parallel to the sagittal plane, in lateral view. (F) Geometric representation of cancellous bone architecture in the lateral tibial condyle of Allosaurus and tyrannosaurids (cf. Part I), in the same view as E. (G) Vector field of $\boldsymbol{\sigma}_1$ in the cnemial crest, shown as a 3-D slice parallel to the coronal plane, in anterior view. (H) Geometric representation of cancellous bone architecture in cnemial crest of Allosaurus and tyrannosaurids (cf. Part I), sectioned in the plane of the crest, shown in the same view as G; blue section lines illustrate primary architectural direction. (I) Vector field of $\boldsymbol{\sigma}_1$ in the cnemial crest, shown as a 3-D slice parallel to the sagittal plane, in medial view. (J) G eometric representation of cancellous bone architecture in cnemial crest of Allosaurus and tyrannosaurids (cf. Part I), sectioned in the plane of the crest, shown in the same view as I. (K) Vector field of $\boldsymbol{\sigma}_3$ in the medial aspect of the fibular head, in medial view. (L) Geometric representation of cancellous bone architecture in the fibular head of Allosaurus and tyrannosaurids (cf. Part I), in the same view as K.

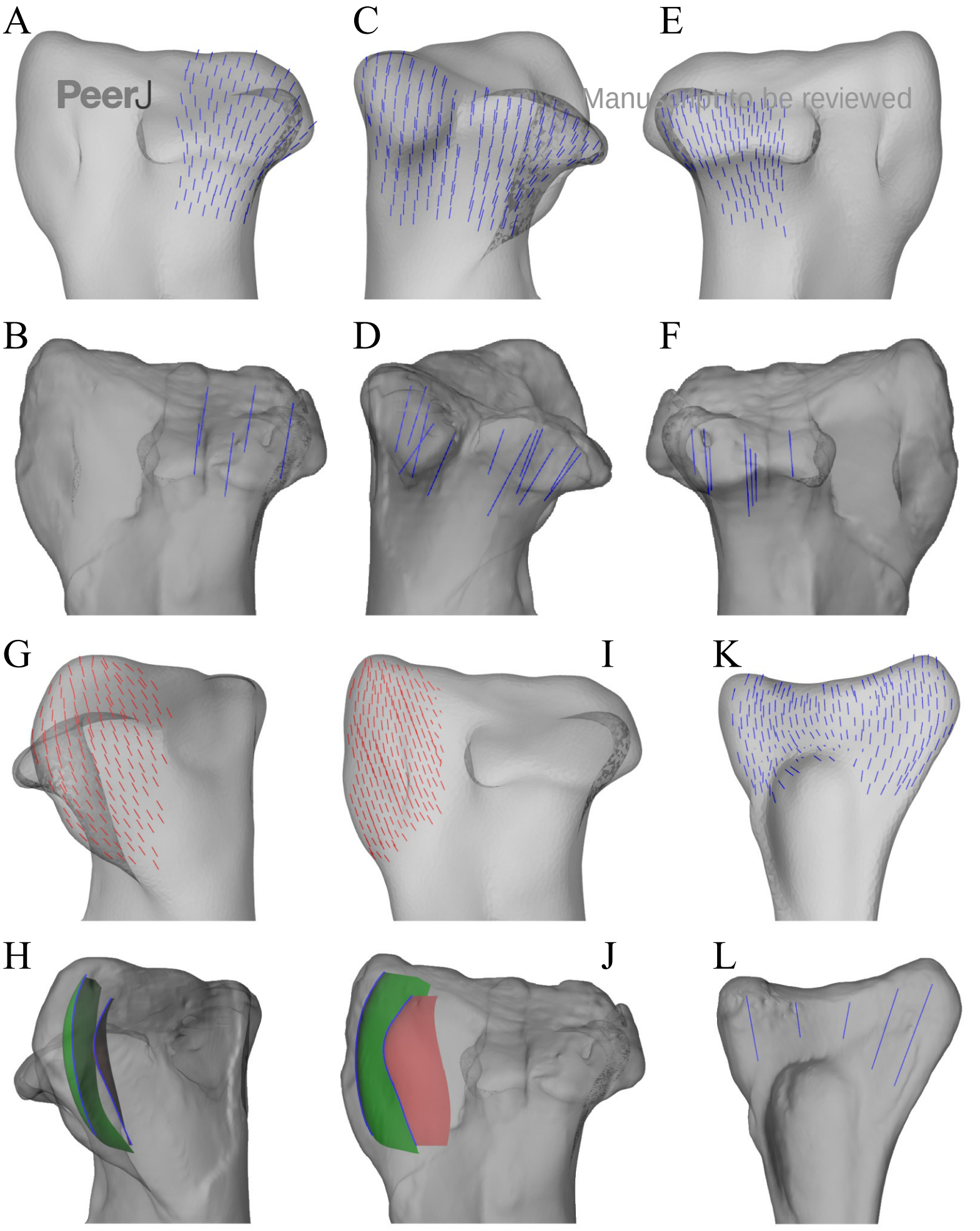

Figure 8(on next page)

Principal stress trajectories for the proximal femurin the solution posture of ‘ Troodon ’, compared with observed cancellous bonefabric.

(A, B) Vector field of $\boldsymbol{\sigma}_3$ in the femoral head, shown as 3-D slices parallel to the coronal plane (A, in anterior view) and sagittal plane (B, in medial view). (C, D) Vector field of $\mathbf{u}_1$ in the femoral head, in the same views as A and B, respectively (cf. Part I) . (E) C omparison of the mean direction of $\boldsymbol{\sigma}_3$ in the femoral head (blue) and the mean direction of $\mathbf{u}_1$ (red), plotted on an equal-angle stereoplot with northern hemisphere projection. Inset shows location of region for which the mean direction of $\boldsymbol{\sigma}_3$ was calculated. (F, G) Vector field of $\boldsymbol{\sigma}_3$ under the greater trochanter, shown as 3-D slices parallel to the coronal plane (F, in posterior view) and sagittal plane (G, in lateral view). (H, I) Vector field of u_1 under the greater trochanter, shown in the same views as F and G, respectively (cf. Part I) . (J) Vector field of $\boldsymbol{\sigma}_1$ in the lesser trochanter, shown in oblique anterolateral view. (K) Vector field of $\mathbf{u}_1$ in the lesser trochanter, shown in the same view as J for both specimens studied (cf. Part I) .

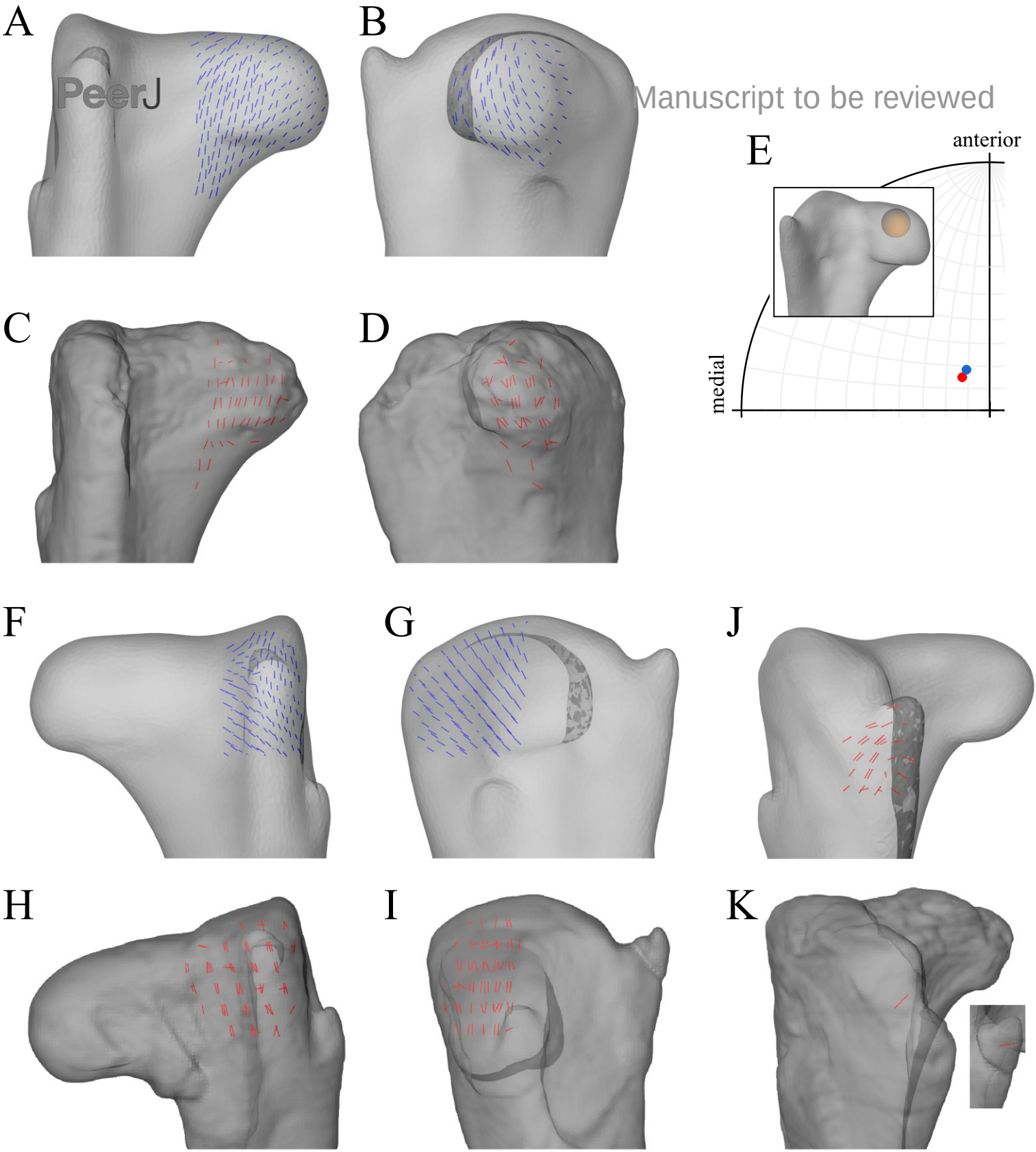

Figure 9(on next page)

Principal stress trajectories for the distal femoralcondyles in the solution posture of ‘ Troodon ’, compared with observedcancellous bone fabric.

(A) Vector field of $\boldsymbol{\sigma}_3$ in the lateral condyle, shown as a 3-D slice parallel to the sagittal plane. (B) Vector field of $\mathbf{u}_1$ in the lateral condyle, shown in the same view as A (cf. Part I) . (C) Vector field of $\boldsymbol{\sigma}_3$ in the medial condyle, shown as a 3-D slice parallel to the sagittal plane. (D) Vector field of $\mathbf{u}_1$ in the medial condyle, shown in the same view as C (cf. Part I) . (E) C omparison of the mean direction of $\boldsymbol{\sigma}_3$ in the medial condyle (blue) and the mean direction of $\mathbf{u}_1$ (red), plotted on an equal-angle stereoplot with southern hemisphere projection. This shows that in the solution posture the mean direction of $\boldsymbol{\sigma}_3$ was of the same general azimuth as the mean direction of $\mathbf{u}_1$, but was markedly more posteriorly inclined. Inset shows location of region for which the mean direction of $\boldsymbol{\sigma}_3$ was calculated.

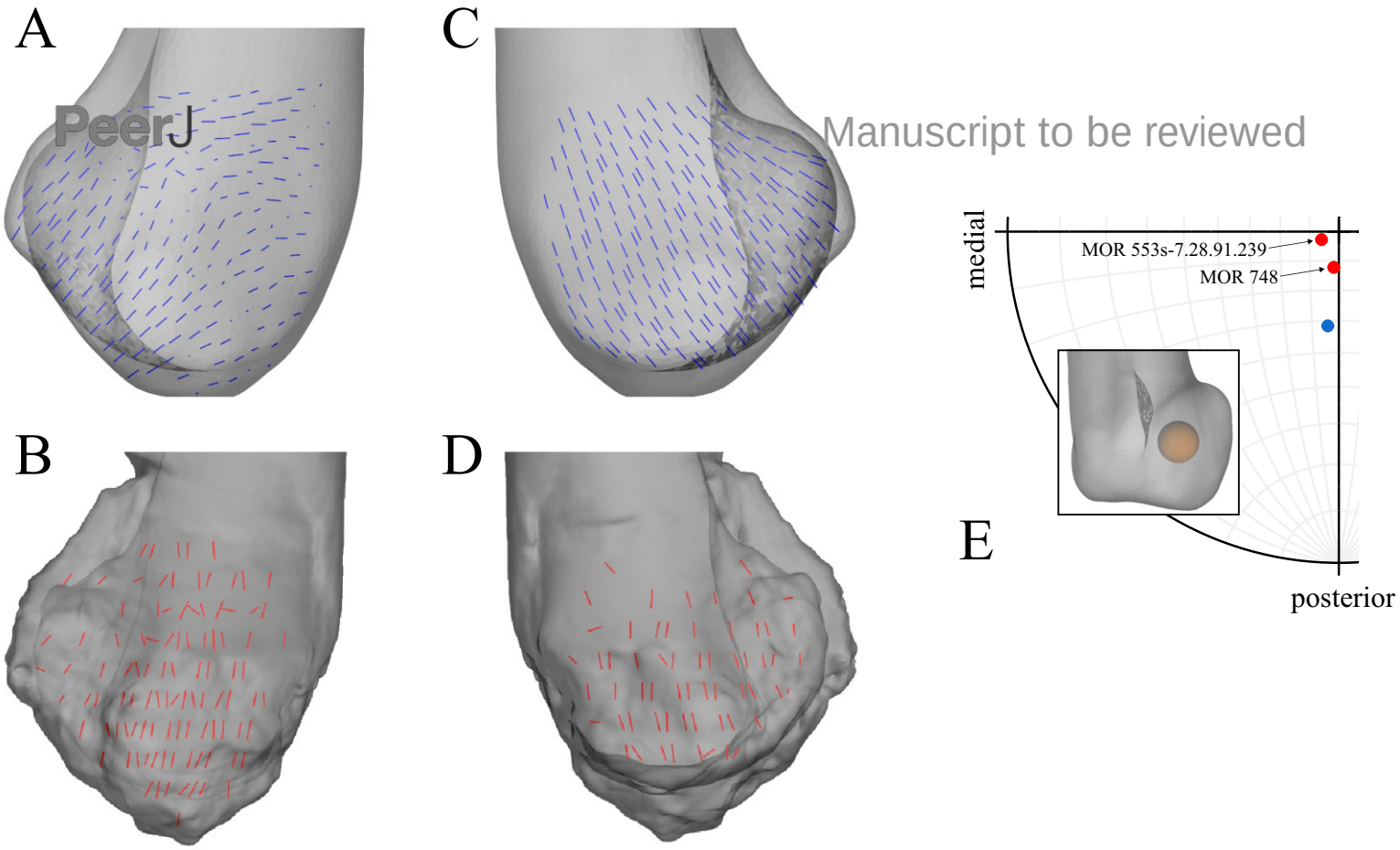

Figure 10(on next page)

Principal stress trajectories for the tibia and fibulain the solution posture for ‘ Troodon ’, compared with observed cancellous bonefabric.

(A) Vector field of $\boldsymbol{\sigma}_3$ in the medial tibial condyle, shown as a 3-D slice through the middle of the condyle and parallel to the sagittal plane, in medial view. (B) Vector field of $\mathbf{u}_1$ in the medial tibial condyle, in the same view as A (cf. Part I) . (C) Vector field of $\boldsymbol{\sigma}_3$ in the medial and lateral tibial condyles, shown as 3-D slices through the middle of the condyles and parallel to the coronal plane, in posterior view. (D) Vector field of $\mathbf{u}_1$ in the medial and lateral tibial condyles , in the same view as C (cf. Part I) . (E) Vector field of $\boldsymbol{\sigma}_3$ in the lateral tibial condyle, shown as a 3-D slice through the middle of the condyle and parallel to the sagittal plane, in lateral view. (F) Vector field of $\mathbf{u}_1$ in the lateral tibial condyle, in the same view as E (cf. Part I) . (G) Vector field of $\boldsymbol{\sigma}_1$ in the cnemial crest, shown as a 3-D slice parallel to the coronal plane, in anterior view. (H) Vector field of $\mathbf{u}_1$ in the cnemial crest, in the same view as G (cf. Part I) . (I) Vector field of $\boldsymbol{\sigma}_1$ in the cnemial crest, shown as a 3-D slice parallel to the sagittal plane, in medial view. (J) Vector field of $\mathbf{u}_1$ in the cnemial crest, in the same view as I (cf. Part I) . (K) Vector field of $\boldsymbol{\sigma}_1$ in the lateral fibular head, in lateral view. (L) Vector field of $\boldsymbol{\sigma}_3$ in the medial fibular head, in medial view (reversed). (M) Vector field of $\mathbf{u}_1$ in the fibular head, in the same view as K (cf. Part I) .

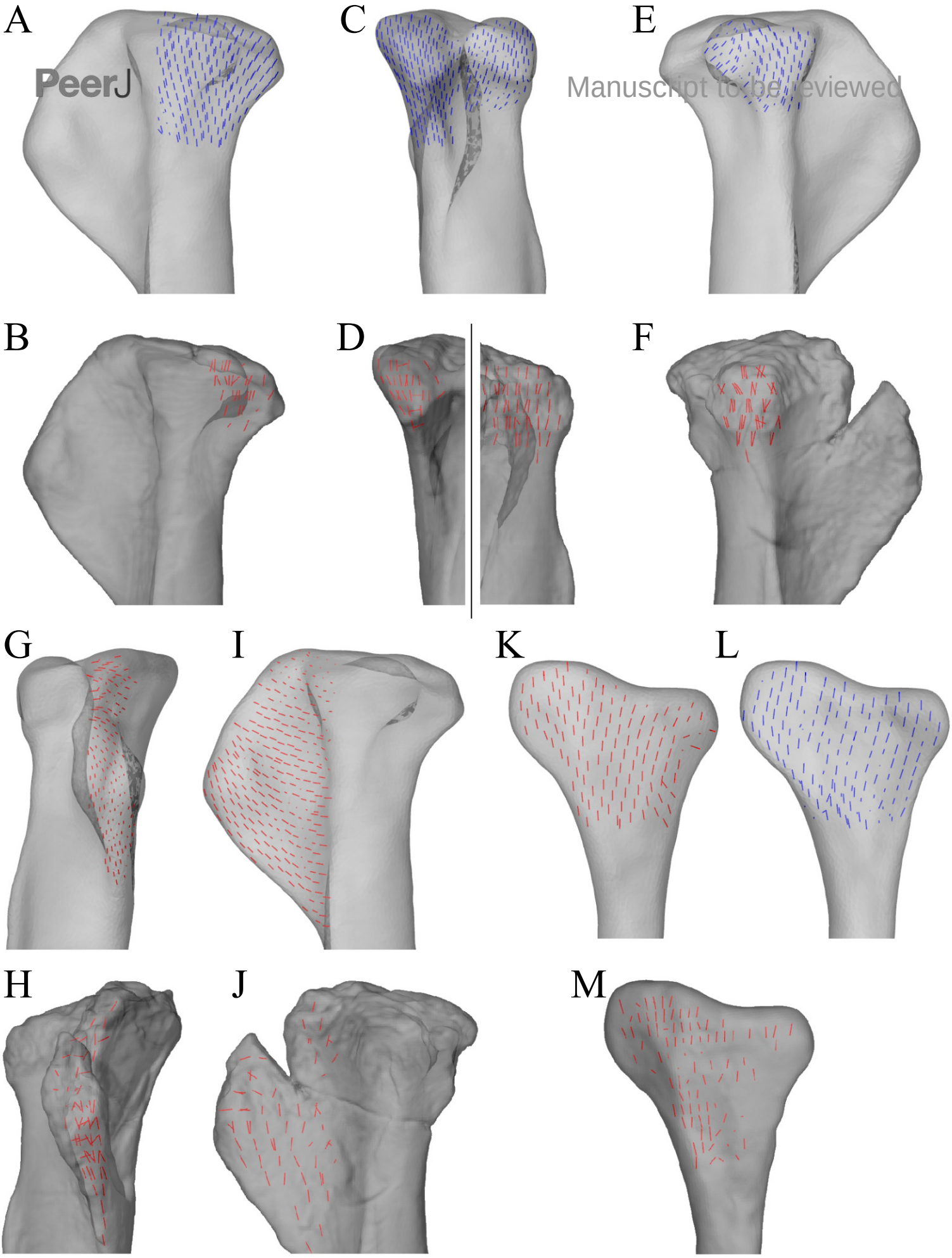

Figure 11 (on next page)

Principal stress trajectories for the proximal femurof Daspletosaurus in the two variations in hip articulation tested.

(A) V ector field of $\boldsymbol{\sigma}_3$ in the first variation tested, shown as a 3-D slice parallel to the coronal plane and through the middle of the femoral head. (B) V ector field of $\boldsymbol{\sigma}_3$ in the first variation tested, shown as a 3-D slice parallel to the sagittal plane and through the apex of the femoral head. (C) V ector field of $\boldsymbol{\sigma}_3$ in the second variation tested, shown as a 3-D slice parallel to the coronal plane and through the middle of the femoral head. (D) V ector field of $\boldsymbol{\sigma}_3$ in the second variation tested, shown as a 3-D slice parallel to the sagittal plane and through the apex of the femoral head. A and C are in anterior view, B and D are in medial view. Note in particular how the trajectory of $\boldsymbol{\sigma}_3$ projects towards the more cylindrical part of the femoral head, lateral to the apex (green braces); compare to Fig. 5A,B,E,F. Also note in **C** how $\boldsymbol{\sigma}_3$ has a strong medial component near the apex of the head.

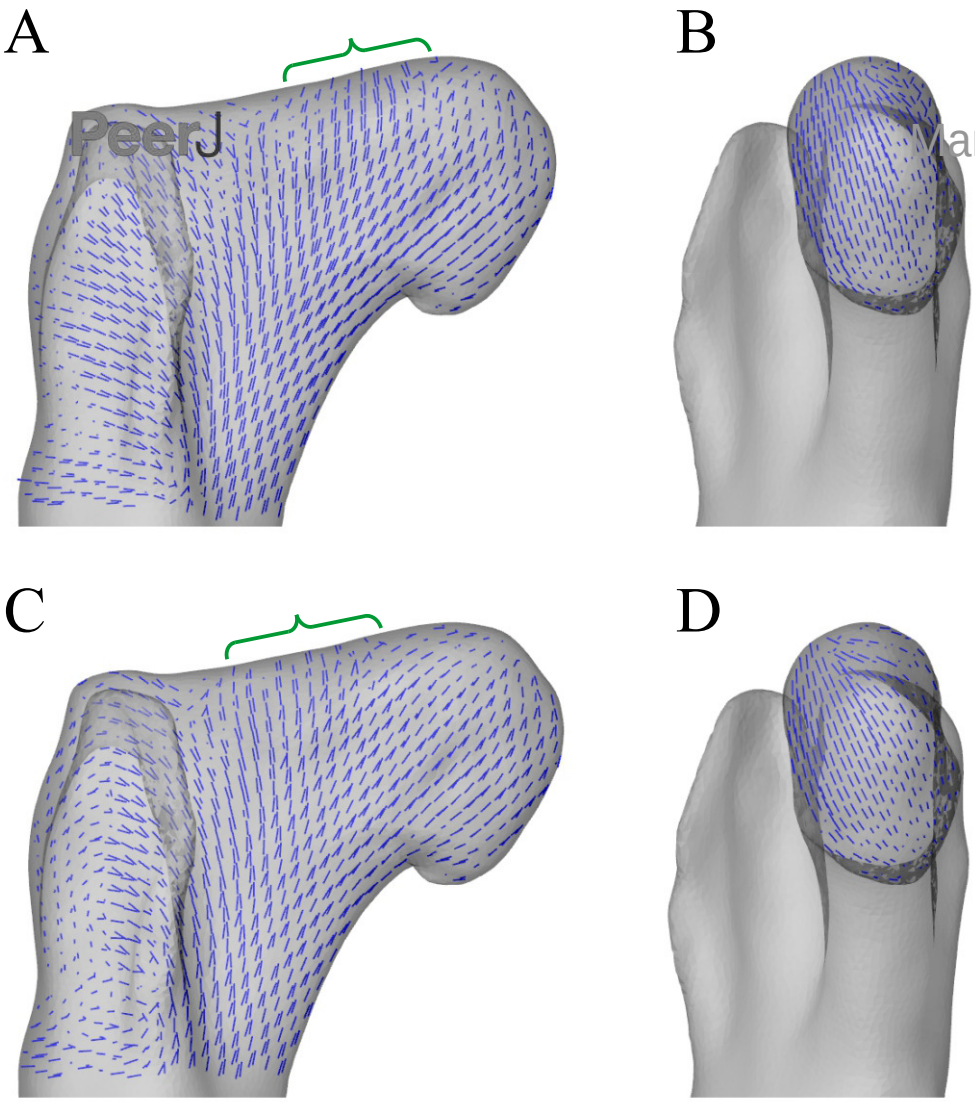

Figure 12(on next page)

Comparison of parameters related to posture, extractedfrom the solution postures of the three species modelled: Daspletosaurus (‘D’),‘ Troodon ’ (‘T’) and the chicken (‘C’).

(A) Schematic illustration of the solution postures retrieved for the three species, along with the location of the whole-body centre of mass (black and white disc). (B) W hole-body centre of mass location anterior to the hips, normalized to total leg length. (C) Degree of crouch for each species, both as measured from the solution posture, as well as empirically predicted from the data reported by Bishop et al. (in review-a) . (D) Angles of the hip and knee joints. The hip extension angle is expressed relative to the horizontal, whereas the knee flexion angle is expressed relative to the femur. (E) Long-axis rotation and adduction-abduction of the hip joint. Positive values indicate external rotation and abduction (respectively), whereas negative values indicate internal rotation and adduction (respectively).

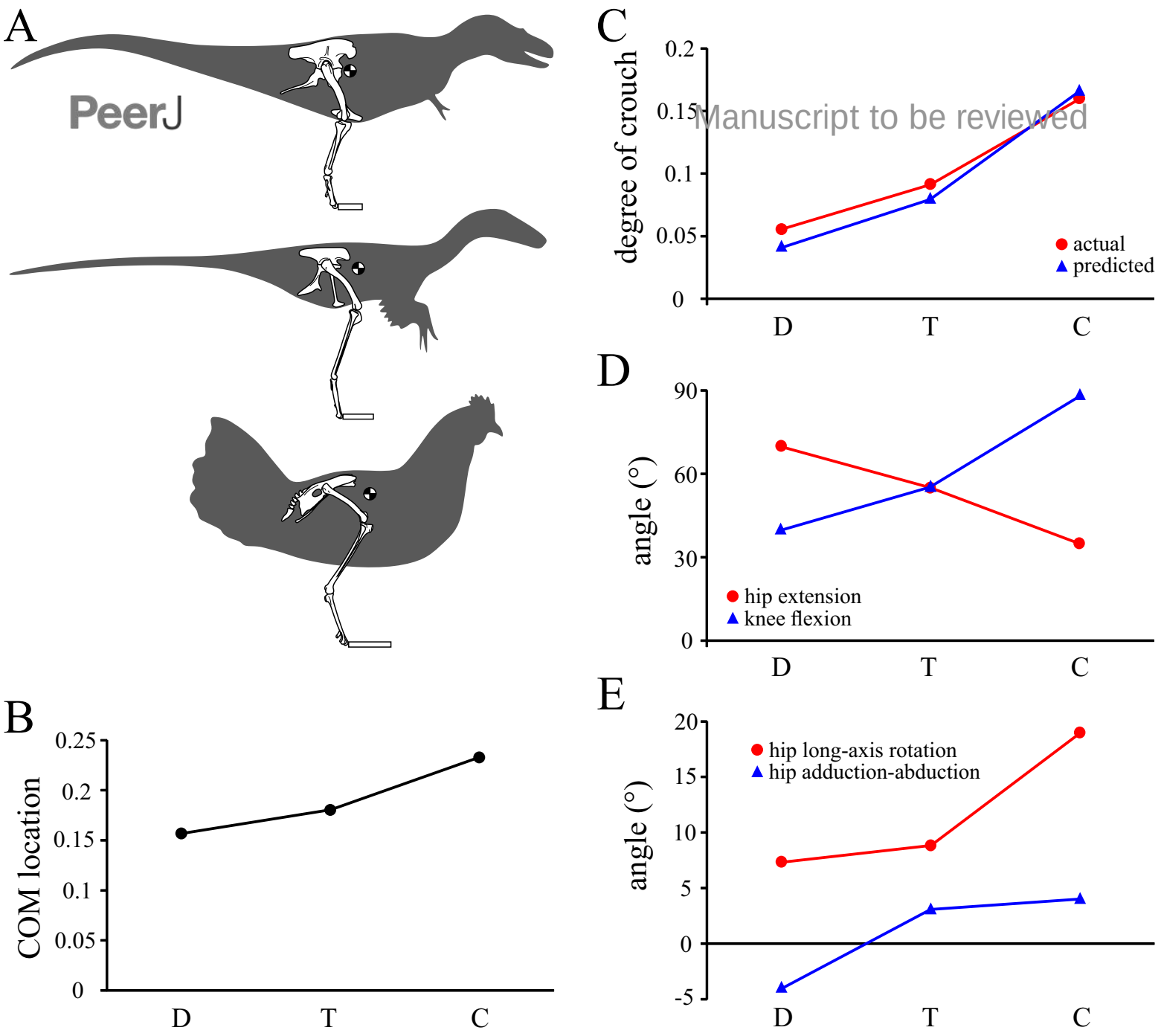

Figure 13 (on next page)

Comparison of parameters related to bone loadingmechanics and muscular support, extracted from the solution postures of thethree species modelled: Daspletosaurus (‘D’), ‘ Troodon ’ (‘T’) and the chicken (‘C’).

(A) Orientation of the neutral axis of bending and the orientation of principal stresses ($\boldsymbol{\sigma}_1$ and $\boldsymbol{\sigma}_3$) relative to the femur long-axis, both measured at mid-shaft. Insets show the neutral axis with respect to the mid-shaft cross-section, as well as anatomical directions (A, anterior; P, posterior; M, medial; L, lateral). (B) Ratio of maximum shear to bending stress in the femoral mid-shaft. (C) Normallized moments of hip abductor and medial rotator muscles. The hip abductor for all species is the iliofemoralis externus (activation set to zero in the chicken; see Part II). In Daspletosaurus and ‘ Troodon ’, the medial rotators are the iliotrochantericus caudalis and puboischiofemorales internus 1 et 2; in the chicken, they are the iliotrochanterici caudalis et medius. (D) Oblique anterolateral view of the hip of Daspletosaurus, showing the abductor and medial rotator muscles (colour codes as in C).